This is a preprint of the following article, which is available from mdolab.engin.umich.edu
Y. Liao, A. Yildirim, J. R. R. A. Martins and Y. L. Young. RANS-based Optimization of a T-shaped Hydrofoil Considering Junction Design. *Ocean Engineering*, 262(2022), October 2022.
The original article may differ from this preprint and is available at
https://doi.org/10.1016/j.oceaneng.2022.112051.

RANS-based Optimization of a T-shaped Hydrofoil Considering Junction Design

Yingqian Liao, Anil Yildirim, Joaquim R. R. A. Martins and Yin Lu Young
Department of Naval Architecture and Marine Engineering, University of Michigan, Ann Arbor, MI, 48109
Department of Aerospace Engineering, University of Michigan, Ann Arbor, MI, 48109
Department of Mechanical Engineering, University of Michigan, Ann Arbor, MI, 48109

Abstract

Hydrodynamic lifting surfaces usually include junctions. High-fidelity simulations are necessary to capture critical physics near these regions, such as separation, junction vortices, and cavitation. We present RANS-based hydrodynamic optimizations of a T-shaped hydrofoil, including changes in the junction geometry. The optimized hydrofoils avoid separation and delay cavitation compared to the baseline. The full optimization design with planform, cross-section, and junction geometry variables yields a total drag reduction of 6.4%. The optimized results show that the relative locations of the maximum foil thickness and the maximum strut thickness significantly impact the junction cavitation. Including the translation between the strut and the foil and more strut geometric variables as design variables will provide further improvement. The comparison between optimized designs demonstrates that optimizing planform and detailed junction geometry provides further improvement in addition to designing the cross-sectional geometry. The hydrostructural analyses show that the optimized T-foils have lower stress at the junction than the baseline because of the resultant junction fairing. However, these hydrodynamic-optimized T-foils have higher deformation and maximum stress, which could result in accelerated fatigue, highlighting the need for hydrostructural responses in design optimization. The results demonstrate that the developed methodology is useful for designing next-generation complex hydrodynamic lifting surfaces.

1 Introduction

Hydrodynamic lifting surfaces, such as propeller blades and rudders, must be attached to other components, such as hubs and hulls. This requirement leads to junctions between the lifting surface and another component, adding to the challenge of hydrodynamic lifting surface design. The shape of the junction affects the pressure and shear stress distribution and thus cavitation inception and flow separation.

Cavitation occurs when the local absolute pressure drops to or slightly lower than the saturated vapor pressure [1, 2]. Once cavitation develops, the periodic cavity shedding may induce material damage because of high local pressure and temperature variations, high shear stress, as well as local shock impact on the structures [3, 4]. Cavitation can also lead to flow-induced load oscillation,

noise, and accelerated fatigue. Hence, avoiding cavitation is crucial to hydrodynamic lifting surfaces when possible, especially composite ones, because composites are less resistant to cavitation pitting damage, even with the current state-of-art coating technology.

Cavitation is tied to flow separation. Flow separation forms a low pressure and low momentum region, which traps microscopic nuclei (weakness in the liquid), allowing cavitation to incept [1, 2, 5].

For marine vessels operating near the free surface, ventilation is another characteristic related to cavitation and separation. Cavitation and separation can both trigger ventilation. Experimental studies have shown that ventilation correlates to boundary layer separation [6, 7]. Ventilation can lead to negative consequences similar to cavitation. Both ventilation and cavitation can lead to sudden and drastic lift (or thrust) loss, efficiency reduction, as well as hydrodynamic and hydroelastic instabilities [5, 8–16]. However, ventilation is fundamentally different from cavitation because it does not involve a phase change. Instead, ventilation is the entrainment of non-condensable gas into the region surrounding the structures, which requires a gas resource to develop the cavity.

Shape optimization, sensing, and control techniques have been used to avoid separation, cavitation, and ventilation [9, 10]. Because junctions are highly susceptible to vortices and cavitation, which can cause pressure fluctuations that lead to performance decay, noise, vibration, surface erosion, and accelerated fatigue [17, 18], a well-designed junction shape is essential for vessels' stability and efficiency.

The junction shape also affects the structural response. Any drastic change in the junction shape can cause stress concentrations, leading to accelerated fatigue and other material failures. Therefore, it is crucial to include the junction details when optimizing hydrodynamic lifting surface performance while avoiding separation, cavitation, ventilation, and structural failure.

Recent advances in manufacturing robots and 3-D printing technology allow cost-effective manufacturing of highly optimized sections, including the junction shape. In the past, metallic materials limited the design freedom at the junction because it depended on the welding technique and quality. For composite materials, conventional manufacturing technologies also made junction optimization challenging. Recently developed methods such as automated fiber placement and 3-D printing enable efficient and accurate manufacturing of optimized hydrofoils with more design freedom. Thus, using these new manufacturing techniques can yield higher-performing lifting surfaces.

These new manufacturing techniques and the need to avoid cavitation and separation motivate the detailed shape design optimization of complex hydrodynamic lifting surfaces. Numerical methods have been developed to optimize hydrodynamic lifting surfaces. Early approaches rely on low-fidelity methods, such as lifting line and panel methods [19–21]. These low-fidelity methods still attract industry and academia because of the low computational cost [22]. More recently, researchers have developed boundary element methods for analyses and designs of hydrofoils and propellers [23–28] Despite that the low-fidelity methods and boundary element methods can capture the trends with low computational cost, high-fidelity simulations are needed to more accurately capture critical physics, such as cavitation and separation [29–31]. In the numerical design optimization context, Reynolds-averaged Navier–Stokes (RANS) model is commonly used because it is currently the highest-fidelity approach that is still computationally tractable [32–37]. However, high-fidelity models are computationally prohibitive for design problems requiring many simulations, particularly for complex multipoint loading.

Fortunately, the adjoint approach mitigates the overall computational cost of optimization when used with a gradient-based optimizer [38–40]. The adjoint approach computes the gradients of a function of interest with respect to a large number of design variables accurately and efficiently. This approach linearizes the simulation and then solves a linear system for each function of interest to compute the entire gradient [41, Sec. 6.6]. There are other methods for computing derivatives, but none are as efficient when the number of design variables is greater than the number of functions

of interest [41, Sec. 6.2]. Kenway et al. [40] provides more details on the implementation of the adjoint approach. In this paper, we use a 3-D RANS and gradient-based optimization framework with an adjoint method to optimize the geometry of hydrodynamic lifting surfaces.

To design hydrodynamic lifting surfaces that intersect with other components, we need 3-D RANS simulations. In addition, we need to be able to change the geometry of the components and their intersection. Computational fluid dynamics (CFD) with the overset mesh approach can handle significant geometry changes and relative movements between components while preserving good mesh quality compared to multiblock meshes [42]. For a geometry with intersecting components, the surface mesh deformation near the junction is challenging because the CFD solver requires the surface mesh nodes to conform with the changed design outer mold lines and maintain the watertight property [43]. Secco et al. [35], Secco and Martins [44] developed a robust algorithm to handle this mesh deformation with overset meshes and demonstrated the advantages of using a wing-body configuration and a strut-braced wing.

We will use a gradient-based optimization framework that uses RANS CFD and overset meshes to design hydrodynamic lifting surfaces with junctions. We use a T-shaped hydrofoil as a canonical example for hydrodynamic lifting surfaces because it features a representative junction geometry that is of current interest. T-shaped hydrofoils are often used for hydrofoil-supported crafts, which have been popular since the mid-20th century, as they can operate at high speeds and have good seakeeping characteristics [45, 46]. The supporting hydrofoils provide lift for vessels to operate with the hull bottom out of the water, reducing the hull wetted area and interaction with waves. Hence, these crafts experience less drag at foil-borne operation conditions and achieve higher maximum speeds with better ride quality. The popularity of hydrofoil-supported crafts dropped since the 1970s because of the limitation on size due to the cube-square law of the weight and lift, the development of high-speed catamarans, propulsion design difficulties, limited material choices, inadequate manufacturing techniques, and mechanical issues caused by the system's complexity. However, recent advances in material technology, manufacturing, numerical modeling, sensing, and control strategies made them attractive again. In addition, the green energy initiative has driven the recent development of hydrofoil-supported vessels because they remain the most efficient water vehicles, resulting in fuel and power consumption reductions.

Hydrofoil designs have been increasingly adopted in competitive sailing communities, such as the International Moth class and America's Cup [47–49]. Three widely used types are L-foils, C-foils, and T-foils. T-foils provide more stable performance and exhibit better control authority because the foils are fully submerged in water. T-foils can also naturally damp wave-induced vessel heave motions [46, 50]. The physics and trade-offs from the canonical T-shaped hydrofoil shape optimization example should also apply to more generic hydrodynamic lifting surface designs with junctions and is thus relevant to propulsion, control surfaces, energy-saving and energy-harvesting devices.

Many efforts simulated and designed hydrofoil crafts and T-foils. Experiments have been an important avenue to understand the physics [8, 11, 12, 51–55]. Scherer and Auslaender [51] presented an early work comparing the experimental lift and drag measurements of a T-shaped Buships parent hydrofoil with the theoretical prediction. They also investigated and discussed the cavitation and ventilation performance of this hydrofoil. Binns et al. [52] conducted experiments to study the effect of heel angle and foil submergence depth on the force of a T-foil. Later, Ashworth Briggs [53] performed a more comprehensive set of experiments on a similar T-foil to study free surface effects on the T-foil forces and tip vortex ventilation. Beaver and Zseleczky [56] performed a series of tests for a full-scale foiling moth, characterizing major parameters that impact the foil, hull, sail, and strut performance. Harwood et al. [8, 11, 12, 55] completed several detailed tests to investigate the ventilation mechanism and hydroelastic response of surface piercing hydrofoils.

In addition to experimental testing, computational methods have also been used to evaluate the performance and trade-offs. Low-fidelity methods are still valuable and have been applied to foil performance prediction for comparing with experimental measurements [54] and for design [22, 57]. Recent advances in computer science and scientific computing promote the use of higher-fidelity methods, such as RANS [32, 34, 37, 58, 59]. However, these previous efforts with high-fidelity approaches mostly only considered a single foil performance. They did not take the presence of the junction and the strut (or other attached components) into account. Hence, we aim to develop methods to complement current research to include the junction design of a foil-strut system in RANS-based design optimization.

Overall, the objectives of this paper are to 1) optimize a T-foil considering a large number of design variables using a high-fidelity adjoint-based optimization framework, and 2) investigate how cross-sectional, planform, and detailed junction geometry design affect the design and performance of the T-foil.

The remainder of this paper is organized as follows: We first introduce and review the computational framework in Section 2. The optimization problem setup is then described in Section 3. We show and discuss the results in Section 4. In Section 4.4, we conclude our findings.

2 Computational framework

We use the MACH framework for the analyses and optimizations [60]. MACH enables the optimization of lifting surfaces with respect to external shape and structural sizing variables while accounting for flexibility [61]. Because we do not include the structural response in the hydrodynamic optimizations in this paper, we use the subset of the MACH framework called MACH-Aero, which consists of the computational tools required to perform aerodynamic or hydrodynamic shape optimization.

Figure 1 shows an overview of the hydrodynamic shape optimization framework. The hydrodynamic shape optimization process starts with the pre-processing step shown in Figure 1, in which the geometry and the computational meshes are generated. We generate the T-foil geometry that will be introduced later in Section 3.1 and the corresponding free-form deformation (FFD) volumes using the pyGeo module [62], which is a geometry manipulation tool for multidisciplinary design optimization that provides convenient ways to manipulate lifting surface geometries. We import the T-foil geometry into the ANSYS ICEM-CFD software and use ICEM-CFD to generate the CFD surface meshes. Finally, the surface meshes are extruded to volume meshes using the pyHyp module [63], which solves hyperbolic equations to determine the volume layer positions. The following sections detail the steps and tools required to perform hydrodynamic shape optimization.

2.1 Geometric parameterization

We use the FFD implementation available in the pyGeo module [65] to parameterize the hydrofoil geometry. With this approach, the CFD surface mesh nodes are embedded in a control volume defined by a set of control points, as shown in Figure 2. The parametric coordinates of the mesh points are mapped to the FFD control points using B-splines. The control points move the mesh nodes through the parametric mapping. Moving each control point allows us to change local variables that control the airfoil shapes. It is also possible to change global variables, such as twist and sweep, by moving groups of control points. The global variables require a reference axis about which the movement takes place. The geometric variables and constraints for the T-foil problem are detailed in Section 3.5.

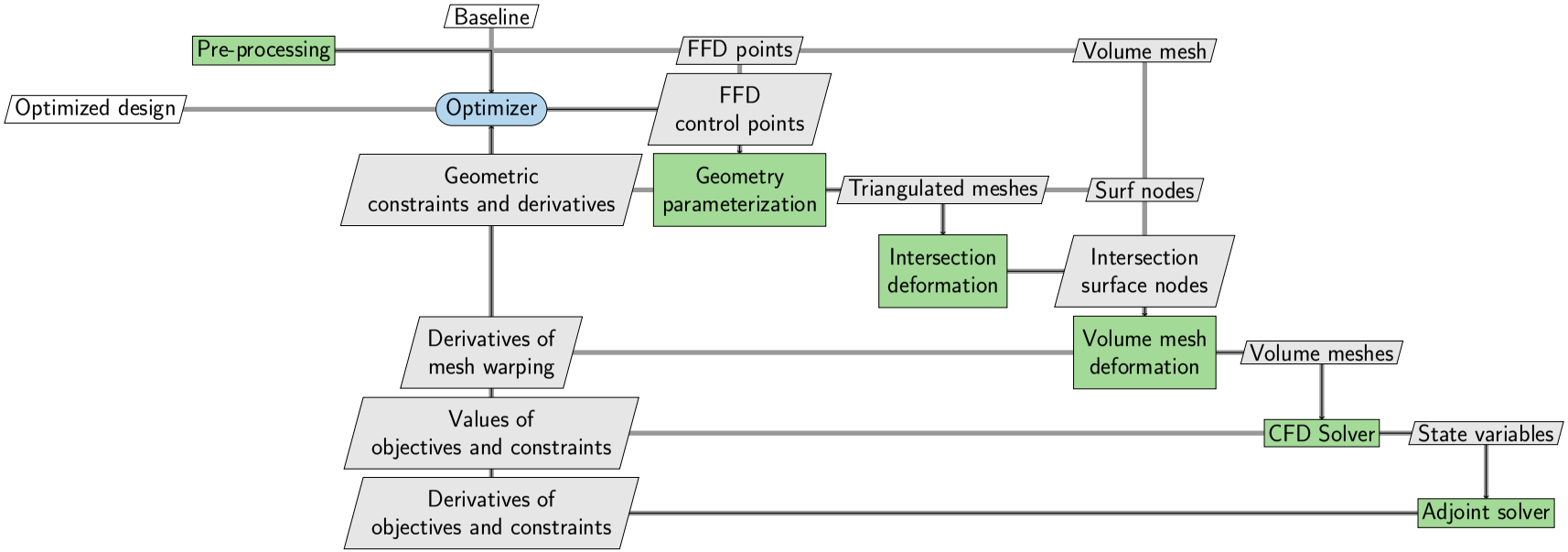

Figure 1: XSDM diagram of hydrostructural optimization with MACH [64]

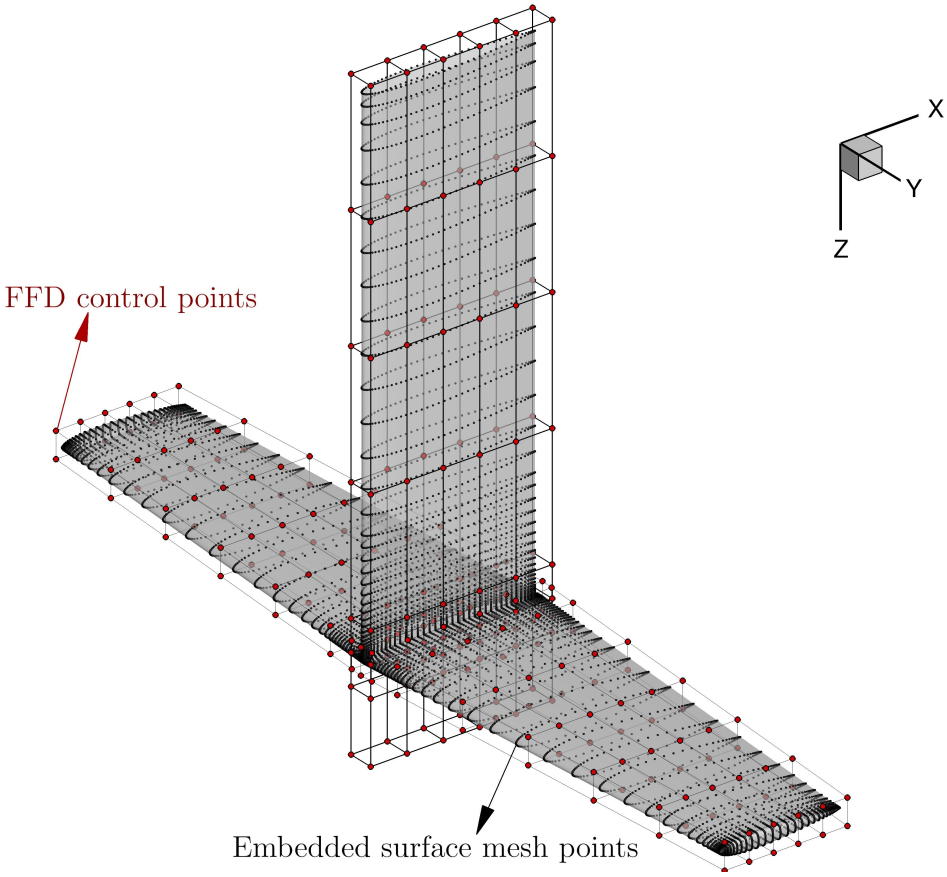

Figure 2: The geometric parametrization uses FFD control points to deform the embedded surface mesh points.

2.2 Multi-component surface mesh deformation

The FFD approach described above is sufficient to update the CFD surface mesh based on the geometric design variables for a standalone component such as a single hydrofoil. However, for a configuration like the T-shaped hydrofoil introduced in Section 3.5, which contains a junction between the foil and the strut, we need an additional step to update the CFD surface mesh based on component junction changes. This step is required to ensure that the CFD surface mesh conforms to the updated design geometry and avoid obtaining invalid volume mesh cells near the junction.

To achieve this goal, we use the surface mesh deformation method developed by Yildirim et al. [43], which is based on the pySurf module developed by Secco et al. [35]. To parameterize the geometry of the configuration that includes multiple components that intersect, we first use separate FFD volumes to parameterize the design of the foil and the strut separately. In addition to tracking the CFD surface mesh with the FFD volumes, we track a triangulated surface mesh for each component to compute the updated junction between the two components as their shapes change. Finally, using the updated junction curve between the two components and the updated feature curves, we use an inverse-distance weighted deformation approach to deform the CFD surface nodes near the junction between components. As a result of these operations, this method updates the CFD mesh to conform with the updated component geometries and the new junction between components. This algorithm has been differentiated analytically for use with gradient-based optimization [35, 43].

2.3 Volume mesh deformation

We deform the CFD volume mesh based on the updated CFD surface mesh computed in the previous step. We use a mesh deformation process to update the CFD volume mesh at each iteration instead of re-meshing. Compared to re-meshing, mesh deformation is more efficient and provides a more consistent geometric representation throughout the optimization.

For the CFD volume mesh deformation process, the surface mesh deformation is propagated to the volume mesh using the IDWarp module developed by Secco et al. [63], who implemented a mesh deformation approach based on an inverse distance weighting method [66]. The corresponding mesh deformation derivatives are computed using automatic differentiation. This mesh deformation process and the derivative computation are fully parallelized and only take about 0.1% of the CFD runtime [63]. The updated CFD meshes are then provided to the CFD solver for hydrodynamic simulation.

2.4 CFD solver

The CFD solver we use in this work is ADflow [67], which is a second-order accurate finite volume solver [39]. ADflow can solve the compressible Euler, laminar Navier–Stokes, and RANS equations with structured multiblock and overset meshes. Because we consider design conditions with chord-based Reynolds number $Re \geqslant 10^6$, we assume the flow studied in this paper is fully turbulent. We solve the steady RANS equations with the Spalart–Allmaras turbulence model [68] in this work unless otherwise specified. We use this turbulence model because it has been differentiated and is ready to be used with gradient-based optimization. We use the overset mesh approach in the CFD simulations because an overset mesh can result in higher quality cells near component intersections compared to a structured multiblock mesh [42]. In our model, the overset mesh approach enables us to create high-quality component meshes for the foil, strut, and the collar, as described in Section 3.2. In the overset approach, cells can be blanked, interpolated, or computed. An implicit hole cutting process determines the role of each volume cell as described by Kenway et al. [42].

We start solving the flow using a Runge–Kutta method and switch to an approximate Newton–Krylov method [69] when the residual drops a certain magnitude relative to the initial free flow

residual. After using the approximate Newton–Krylov solver to lower the residual quickly, a pure Newton–Krylov solver performs the final convergence, further accelerating the overall solution. The selection of different nonlinear solver algorithms does not have any effect on the final converged solution; we use different nonlinear solvers in different simulation stages to accelerate the process of finding a steady-state solution. Following the flow solution, we use the adjoint method in ADflow implemented by Kenway et al. [40] to obtain the derivatives across the CFD solver efficiently.

As previously alluded to, cavitation can lead to significant efficiency deterioration, material surface erosion, and cavity-induced vibrations. Although the CFD solver cannot simulate actual cavities, it can impose a cavitation constraint using a metric based on local pressure. Similarly, the CFD solver can impose separation constraints based on the local flow direction. We explain the cavitation and separation constraint formulations in Section 3.6.

3 Optimization problem setup

In this section, we will first describe the baseline, for which the geometry details are summarized in Table 1. Afterward, we describe how we generate the CFD meshes and the boundary conditions. We present a validation study in Section 3.4. Design variables and constraints are described in Sections 3.5, 3.6, and 3.7. Section 3.8 describes the optimization problem formulation, including two tables summarizing the design conditions (Table 3) and the optimization problem (Table 4).

3.1 Baseline design

We use a T-foil design from [53] as the baseline hydrofoil. This baseline is a canonical representation of a T-foil rudder for the International Moth Class [47]. The T-foil has a semi-span (b) of 0.333 m, a root chord (c_{root}) of 0.14 m, and a tip chord (c_{tip}) of 0.095 m, as shown in Figure 3. In our simulations, we use a strut chord of 0.135 m to reserve space for creating a qualified collar mesh near the trailing edge. These geometry details are also summarized in Table 1. We immerse the foil at a water depth (h) of 0.4 m from the free surface (measured at leading edge), which results in a depth-to-mean-chord ratio (h/c_{mean}) of 3.4. Both the baseline strut and foil geometries have NACA 0012 cross-sections (the strut cross-section may differ from the original work of Ashworth Briggs [53] because the strut cross-sectional geometry was not reported, but it should have only a minor impact on the foil performance).

Table 1: Geometry details of the baseline.

Cross section	NACA 0012
Submergence depth	0.4 m
Strut chord	0.135 m
Foil root chord	0.14 m
Foil tip chord	0.095 m

The baseline cross-section is not optimal for a lifting surface that is susceptible to cavitation and ventilation. We choose this model because there are experimental results to compare against, and it is a relatively simple baseline geometry to replicate [52, 53]. Additionally, for a well-defined optimization problem, the choice of baseline shape should have a negligible impact on the optimized geometry in the absence of multimodal solutions. Previous work has shown that with adequate problem formulation, optimizations starting from different initial designs converge to essentially

the same optimized shape [70, 71]. Therefore, the baseline design is not likely to affect the optimal designs for this problem.

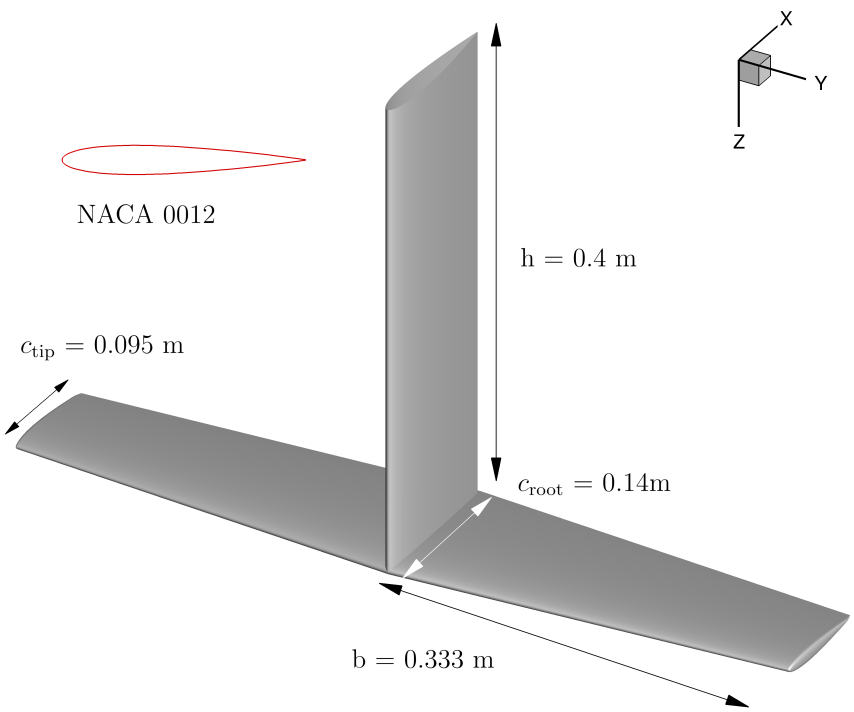

Figure 3: Baseline T-foil design dimensions.

3.2 CFD mesh

The overset mesh for the T-foil consists of a mesh for the lifting surface, a mesh for the strut, and a collar mesh, as shown in Figure 4. The collar mesh is required to ensure adequate discretization to resolve the boundary layer at the junction. The overset mesh uses an implicit hole cutting process to determine the CFD cell role [72]. CFD cells can be blanked, interpolated, or actual compute cells. We generate two levels of CFD meshes to assess the mesh dependency. For the coarse mesh, the strut surface mesh has 1,944 cells, the collar has 3,888 cells, and the foil has 15,024 cells. The surface meshes are extruded 0.2 m in the normal direction to generate volume meshes, as shown in Figure 4. The foil and the strut volume meshes have 32 cells in the normal direction. On the other hand, the collar has 40 layers to provide a smaller extrusion grid ratio (1.2951) than the strut and foil (1.3916) so that collar cells are prioritized during the implicit hole cutting process. The volume meshes of individual components and the final combined mesh for the coarse mesh are shown in Figure 4. These component meshes are combined with a background mesh to form the final overset mesh. The background mesh is an O-grid that contains a Cartesian grid bounding the T-foil volumes and the extrusion to the outer boundary. The final coarse mesh has a total of 991,712 volume cells. After the implicit hole cutting process, there are 891,112 compute cells. The final coarse mesh has a maximum y^+ of 2.7 at the nominal design condition with $Re = 1.6 \times 10^6$ and a maximum y^+ of 3.2 at the highest speed condition with $Re = 2.1 \times 10^6$. The design conditions are described in Section 3.8.

The fine mesh is generated following the same process. The fine mesh has 7,456,768 cells in

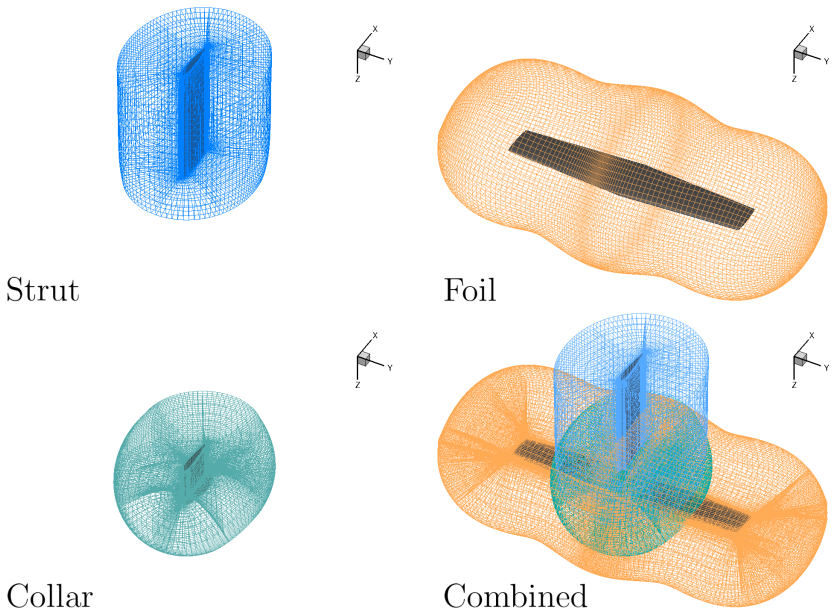

Figure 4: Volume meshes for each component and the final combined volume mesh without the background mesh.

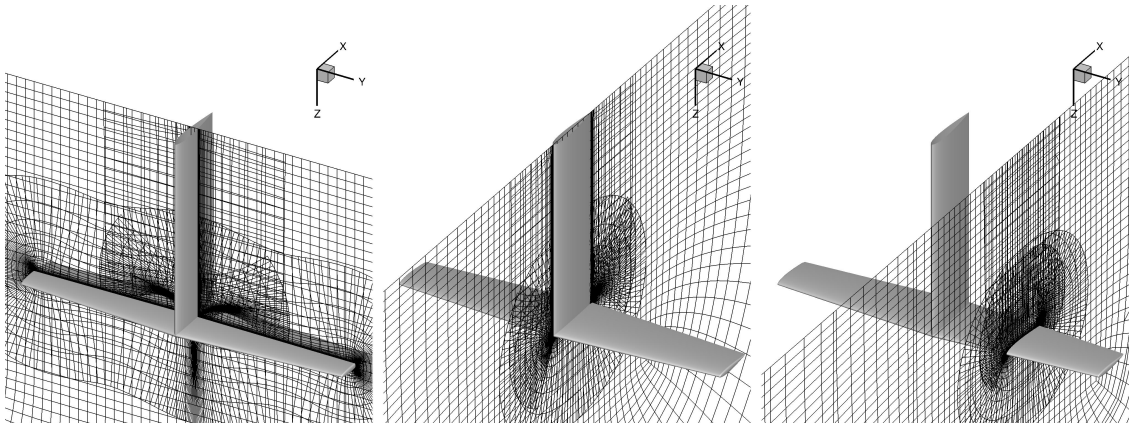

(a) Volume mesh slices through the planes perpendicular to the horizontal foil.

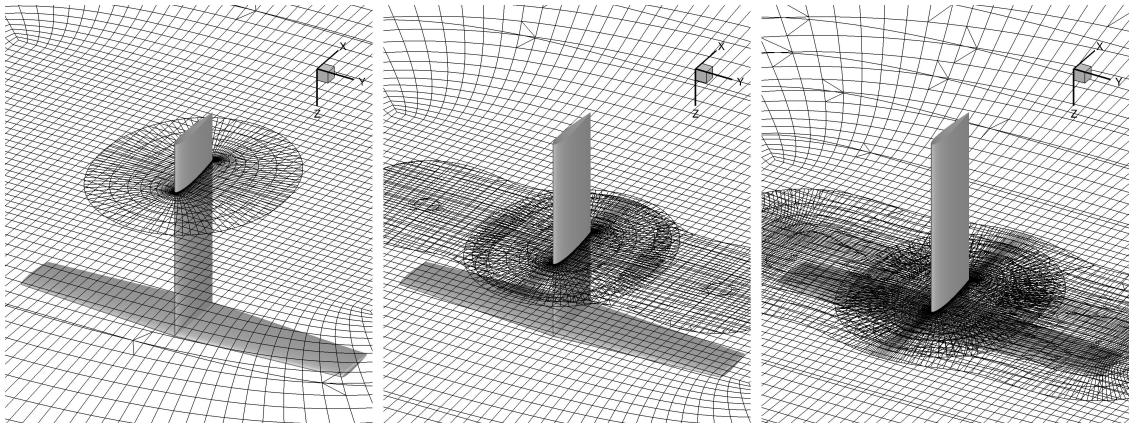

(b) Volume mesh slices through the planes perpendicular to the vertical strut.

Figure 5: Slices of the final coarse mesh including the background mesh.

total with a maximum y^+ of 1.2 at the nominal design condition. The discretization number in each dimension doubles compare to the coarse mesh. We decrease the fine mesh's off-spacing to half of the coarse mesh when creating the volume mesh. For the collar mesh, the normal extrusion distance is 0.15 m compared to the 0.2 m used for the coarse mesh to ensure a valid final overset mesh. The normal marching distance for the foil and strut volume mesh remains the same as the coarse mesh. After the implicit hole cutting process, the fine mesh has 6,910,434 compute cells. Figure 6 shows the surface compute cells with zipper meshes for both the coarse and fine mesh levels.

In this work, we did not apply any mesh refinement around the tip region to investigate the tip leakage flow in detail. Our focus is on the developments that enable junction shape design for complex hydrodynamic lifting bodies. However, tip leakage flow can significantly impact the hydrofoil performance, such as inducing downwash, triggering cavitation, and ventilation. Tip mesh refinement analyses could be performed in the future to ensure the tip vortices are appropriately captured. Example avenues include using a C-mesh and applying local mesh refinement near the tip.

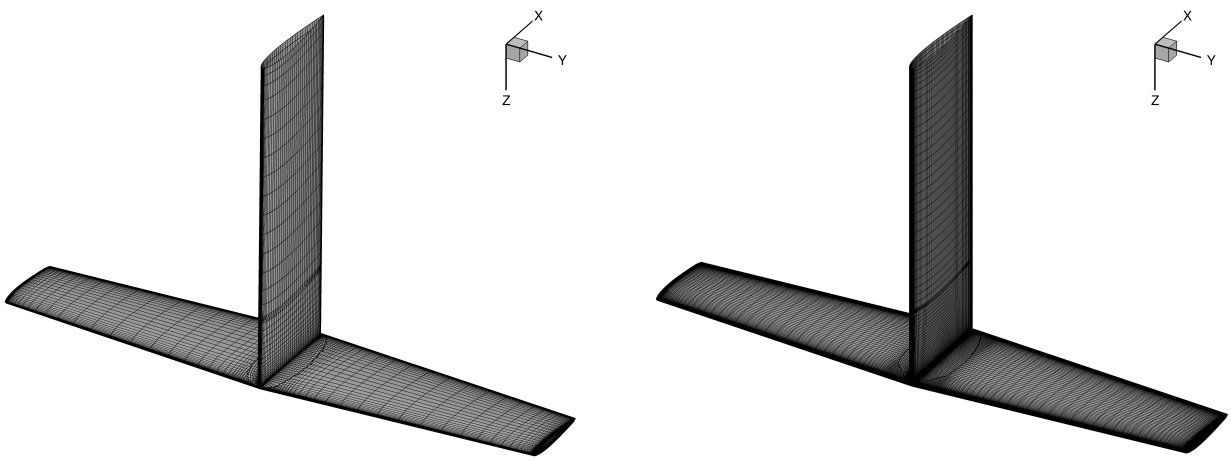

(a) Coarse mesh with 891,112 compute cells. **(b)** Fine mesh with 6,910,434 compute cells.

Figure 6: Surface compute cells for the coarse (a) and fine (b) mesh levels, including the zipper meshes.

For this T-foil problem, the drag coefficient (C_D) and lift coefficient (C_L) are defined as the total (foil and strut) drag and total lift non-dimensionalized by the dynamic pressure and the reference area of the horizontal foil ($A_{\text{ref}} = 0.0783\ m^2$), which is the product of the mean chord and the span. Later in the results, we report the total drag and the drag for different components separately. Figure 12 shows how we group surfaces for each component.

3.3 Boundary conditions

We apply symmetry plane boundary conditions at the top of the strut and far-field boundary conditions at about nine span lengths away from the bounding Cartesian mesh. The symmetry boundary condition corresponds to the low speed, i.e., low submergence-based Froude number ($Fn_h = U/\sqrt{gh}$) condition, or when the strut is connected to the bottom of the hull and is fully wetted.

At low Fn_h limits, the lift increases when approaching the free surface; at high Fn_h conditions,

the lift decreases when approaching the free surface. Ashworth Briggs [53] observed that for the T-foil, both lift and drag forces approach an asymptote at an h/c_{mean} of 1.7 at 2 m/s, which corresponds to $Fn_h = 1.4$. Hence, the free surface effect on the steady force is minimal and can be neglected at the h/c_{mean} value of 3.4 used in this work.

To verify that the symmetry plane boundary condition effect is small on the T-foil in our simulations with $h/c_{\text{mean}} = 3.4$, we perform analyses with the coarse foil mesh at four different submergence depth values (h) by varying the distance between the foil and the symmetry plane at 4° angle of attack. These simulations include only the foil geometry and mesh; they do not include the strut mesh. Figure 7 demonstrates the relative position between the symmetry plane and the foil for each case. The C_L and C_D values for each case are listed in Table 2.

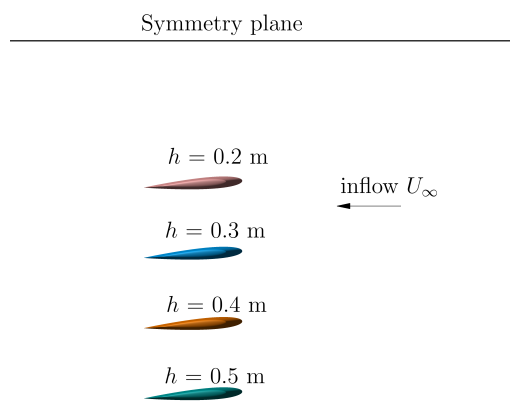

Figure 7: Foil position for each case at different distances from the symmetry plane.

Table 2: C_L and C_D values for four cases at different depths.

		$Re = 1.6 \times 10^6$		
h m	h/c_{mean}	Fn_h	C_L	C_D
0.2	1.7	10.0	0.311745	0.020016
0.3	2.6	8.1	0.301473	0.019865
0.4	3.4	7.1	0.298777	0.019821
0.5	4.3	6.3	0.297208	0.019862

The results show that, at an h/c_{mean} of 3.4, the predicted lift and drag forces approach an asymptote, which means that the symmetry plane effect is small on the foil. The difference between the case with $h/c_{\text{mean}} = 3.4$ ($h = 0.4$ m) and the case with $h/c_{\text{mean}} = 4.3$ ($h = 0.5$ m) is only 0.5% for C_L and 0.2% for C_D with the symmetry plane boundary condition. The symmetry plane effect on the foil steady forces is small at the designed depth (h) of 0.4 m. Therefore, using a symmetry plane boundary condition is an acceptable option for the current problem setup as a simplification and a first step. At the current design water depth ($h/c = 3.4$), it is also assumed that the mean free surface has negligible effects on the pressure distribution and hence cavitating inception is affected by the local absolute hydrostatic pressure only. Parkin et al. [73] observed that when h/c becomes larger than two, the dynamic pressure distribution on the hydrofoil does not vary much. Although their observation was limited to relatively low speeds, the large discrepancy between the current design h/c and the previously investigated h/c value conserves enough margin for our assumption

to be valid. However, we recommend a similar study at high-speed operating regimes in the future. Other than steady forces and mean free surface effects, the free surface can interact with the tip vortices and wake to affect the hydrofoil performance [53]. More appropriate boundary conditions should be considered for more general hydrofoil operations.

3.4 Validation

As a preliminary comparison study, we perform analyses at $U_\infty = 4$ m/s, which results in a Reynolds number of 0.45×10^6 based on the mean chord, and compare the numerical results with available experimental data ($Re = 0.48 \times 10^6$) presented by [53].

The comparison of the numerical results and experimental data is shown in Figure 8. We compare results using both the coarse mesh and the fine mesh. As shown in Figure 8, the coarse mesh underestimates the lift and overestimates the drag. As expected, the fine mesh compares more favorably to the experiments.

The C_D results in Figure 8 show an increasing discrepancy between the fine mesh data and experimental data for both low and high angles of attack. There are two main reasons for this. The first is the lack of a laminar to turbulent transition model in our simulations at low angles of attack. Experiments for angles of attack less than 5° exhibit laminar flow [52], but our simulations assume fully turbulent flow. At low angles of attack ($\alpha \leqslant 4^\circ$) and at low speeds ($Re = 0.48 \times 10^6$ in the experiment), flow is laminar and laminar separation is limited for the chosen NACA 0012 cross-section. Hence, the experimental data and the laminar result show lower C_D than the fully turbulent results at low angles of attack. To investigate this further, we perform a simulation with laminar Navier–Stokes equations at $\alpha = 0^\circ$ with the fine mesh. This laminar result (shown in diamond symbol) in Figure 8 is closer to the experimental data, which leads us to the conclusion that the fully turbulent assumption is likely the cause of the discrepancy at $\alpha \leqslant 4^\circ$. At high angles of attack, laminar separation might happen, and hence the drag increases significantly and exceeds the turbulent simulation results. Additionally, the simulations underestimate the lift, as shown by the C_L results in Figure 8. As s result, the lift-induced drag is underestimated in the high angle of attack range. Other factors contribute to the discrepancy between our numerical data and experimental data. For example, the geometries can vary slightly, such as the junction treatment, the strut chord, and the foil and strut trailing edge thickness values. Nevertheless, if we compare the C_L-C_D results, the fine mesh results match well with the experimental data for $\alpha > 4^\circ$.

From the C_L-C_D plot in Figure 8, the trends (gradients) are similar in the $C_L \geqslant 0.3$ regime between the coarse and the fine meshes. The fine mesh simulation for the baseline geometry is four times more time-consuming than the coarse mesh simulation for the baseline geometry at the angle of attack $\alpha = 1^\circ$. Despite the more accurate predictions given by the fine mesh, we use the coarse mesh in later optimization for a more manageable computational cost.

3.5 Geometric variables and constraints

The geometric design variables include twist distribution, shape variables, and planform variables for the foil, which are shown in Figure 9. The planform variables correspond to the chord and sweep of the foil. The red dots shown in Figure 9 are the FFD control points. We distribute the streamwise FFD points uniformly. In the spanwise direction, we employed more control points near the junction to have better control of the geometry manipulation, as shown in Figure 9. On the outboard portion, the control point distribution is uniform.

The chord variables are defined relative to the reference axis at 0.1% chordwise position to keep the leading edge straight as the design changes. Another reason for defining chord variables with respect to the leading edge is to keep the position of the strut leading edge and foil leading-edge

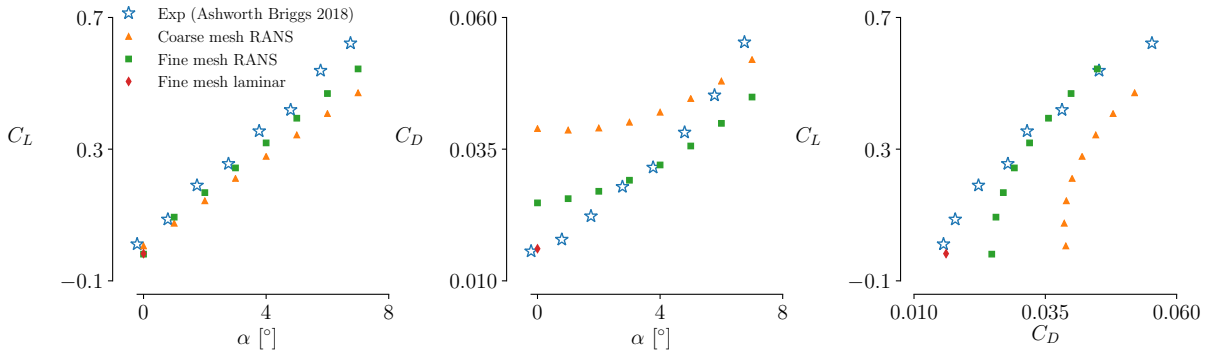

Figure 8: Comparison of numerical predictions and experimental data for the T-foil. The experimental data are shown in open blue star symbols.

fixed relative to each other. As a result, the junction that connects the foil and the strut leading edges remains valid, and the CFD mesh remains water-tight during the optimization. There are three chord variables for the foil and one for the strut. Using a different reference axis for chord variables can shift the foil's leading edge from the strut, leading to an invalid junction line. A linear constraint keeps the strut chord consistent with the foil root chord. The foil chord values are linearly interpolated between the three chord variable stations. A monotonic decrease in the chords is enforced from the center of the foil to the tip.

Using the FFD approach, we define twist variables to control the rotation of the FFD sections about the reference axis, as shown in Figure 9. Since all global geometric variables defined on the one FFD volume share the same reference axis, the twist distribution is also defined relative to the reference axis at 0.1% chordwise position from the leading edge. While only three rotation arrows are shown in the figure to demonstrate the twist sections, we consider the twist variation for each spanwise segment in the optimization. Given the foil symmetry, there are eight twist variables in total.

Sweep is also defined relative to the reference axis at 0.1% chordwise position from the leading edge. The sweep variable λ moves the FFD sections along the streamwise direction, except for the three sections at the junction. This is because shearing two adjacent sections relative to the middle section can cause an invalid junction and a failed mesh.

We change the cross-sectional shapes by moving FFD control points vertically. We separate the top control points from the bottom ones for the three middle sections because we constrain the movement of these control points in some optimization cases to limit the design freedom on the junction shape. We also conduct an optimization without this constraint on the junction shape variables to investigate how designing the junction geometry improves performance.

The span variable stretches the spanwise position of the control points, elongating or shortening the foil span accordingly. The rake variable emulates the angle of attack of the entire T-foil. It is fixed to zero at the cruising condition and only has nonzero values at other flow conditions. We use thickness constraints, leading-edge and trailing-edge constraints to ensure a practical geometry for the optimal design, as illustrated in Figure 10. Finally, the projected area is constrained to ensure that the foil loading is consistent with the overall craft design.

3.6 Cavitation constraint

We use the cavitation constraint as described in our previous work [36]. The cavitation sensor is visualized in Figure 11. Cavitation occurs when the local absolute pressure is lower than the

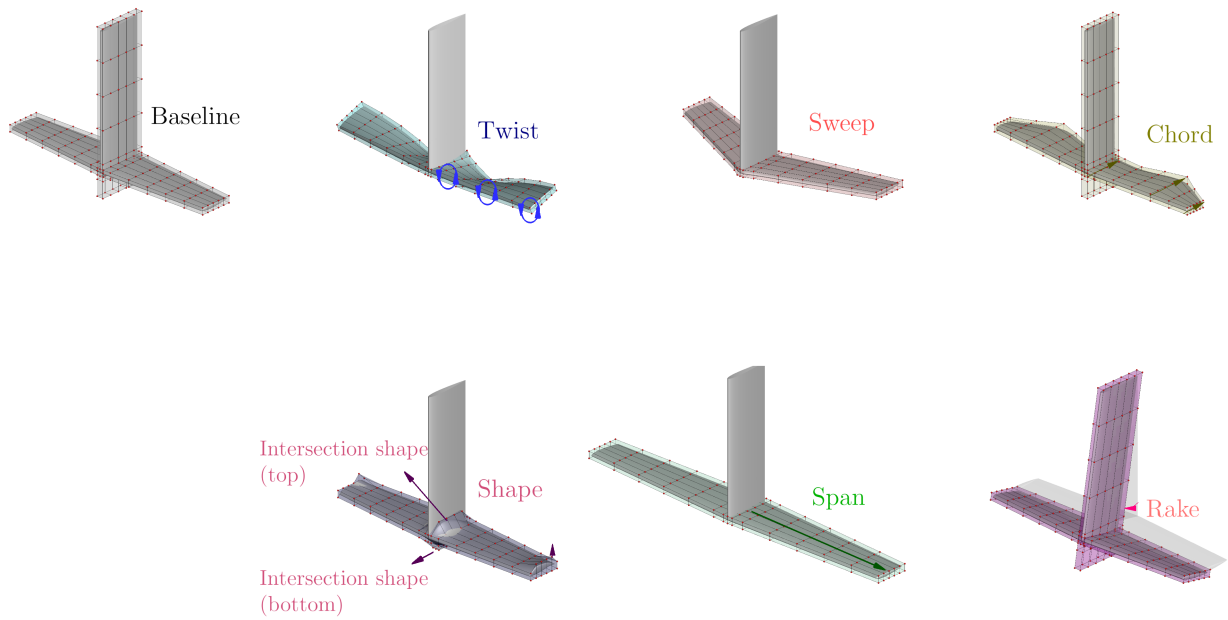

Figure 9: Geometric design variables.

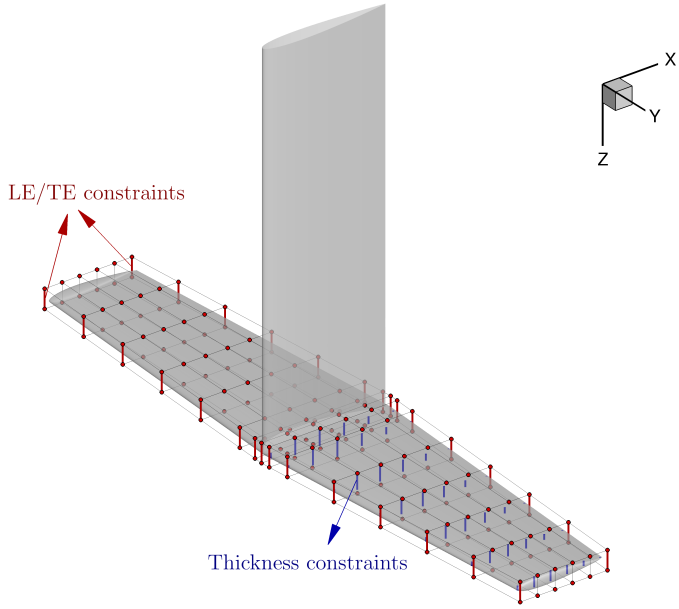

Figure 10: Thickness constraints and leading- and trailing-edge constraints.

saturated vapor pressure, which is equivalent to the negative pressure coefficient $-C_p$ being higher than or equal to the cavitation number σ,

$$-C_p \geqslant \sigma. \tag{1}$$

The cavitation sensor X is defined as

$$X = \begin{cases} 1 & \text{if } -C_p \geqslant \sigma \\ 0 & \text{if } -C_p < \sigma \end{cases}. \tag{2}$$

This is a local quantity that can be computed for each CFD surface cell. To penalize more on the cells with high $-C_p$ values and avoid negative function values, we use $(-C_p - \sigma)^2$ as the penalty weight in the smoothed Heaviside function [36],

$$\bar{X} = \frac{(-C_p - \sigma)^2}{1 + e^{2k(C_p + \sigma + \gamma)}}, \tag{3}$$

where k is a free parameter that determines the transition sharpness and γ is a free parameter that determines the transition shift. The cavitation constraint uses a sharpness (k) value of 10 and an offset (γ) value of 0.2.

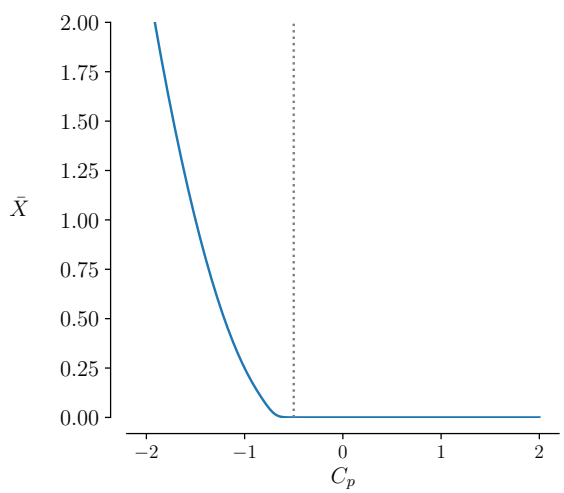

Figure 11: Cavitation sensor used for the T-foil optimization.

The cavitation constraint is formulated as the integral of $\bar{X}$ over the hydrofoil surface except for the trailing edge surface due to numerical oscillations, which represents the total weighted surface area that is susceptible to cavitation.

$$\bar{A}_{\text{cav}} = \frac{1}{2A_{\text{ref}}} \int_A \bar{X} dA, \tag{4}$$

where $A_{\text{ref}} = 2bc_{\text{mean}}$ is the reference area, which is the product of the mean chord and span b, and $\bar{A}_{\text{cav}}$ is the non-dimensional weighted cavitation-inceptive area. The cavitation sensor does not go to zero, and thus we cannot enforce $\bar{A}_{\text{cav}} \leqslant 0$. Instead, we require

$$\bar{A}_{\text{cav}} \leqslant 2 \times 10^{-5}. \tag{5}$$

We scale both sides of this weighted cavitation-inceptive area constraint again by this limit value 2×10^{-5} to formulate the actual constraint value used in the optimization,

$$\frac{\bar{A}_{\text{cav}}}{2 \times 10^{-5}} \leqslant 1. \tag{6}$$

This reformulation provides a constraint value around the order of one to make the optimization problem well-posed. The cavitation constraints are only enforced on the foil surface because we only consider shape variables for the horizontal foil.

3.7 Separation constraint

We use the separation constraint formulation developed by Kenway and Martins [74]. This constraint uses flow reversal as the flow separation indicator. We assume that flow separation occurs if the streamwise component of the flow velocity on the surface becomes negative. The streamwise component is computed using

$$\cos\theta = \frac{\vec{U} \cdot \vec{U}_\infty}{|\vec{U}||\vec{U}_\infty|}, \tag{7}$$

where $\vec{U}$ is the local surface velocity and θ defines the angle between the local surface velocity and the inflow velocity $\vec{U}_\infty$. When $\cos\theta$ becomes negative, i.e. when a reverse flow is detected, the separation sensor is active, which is defined as

$$X = \begin{cases} 1 & \text{if} \quad \cos\theta \leqslant 0, \\ 0 & \text{if} \quad \cos\theta > 0. \end{cases} \tag{8}$$

Similarly to the cavitation constraint, we use a smooth Heaviside function to blend the discontinuity of this original separation sensor to make it suitable for gradient-based optimization. The smooth Heaviside function is given as

$$\bar{X} = \frac{1}{1 + e^{2k(\cos\theta + \gamma)}}, \tag{9}$$

where k and γ are parameters that determine the sharpness of the transition and the shift of the function, respectively. The separation constraint uses a sharpness (k) value of 10 and an offset (γ) value of 0.2. The separation sensor is integrated over a defined region where separation is likely to occur. We then normalize this integral by the reference area, $A_{\text{ref}} = 2bc_{\text{mean}}$, to yield the final separation constraint metric,

$$\bar{A}_{\text{sep}} = \frac{1}{2A_{\text{ref}}} \int \bar{X} dA. \tag{10}$$

We exclude the leading edge, the tip, and the front of the junction in the separation constraint integration because negative streamwise velocity can naturally occur in these regions but does not necessarily indicate flow separation. The surface where we apply the separation constraint is the orange portion of the foil surface shown in Figure 12b. Like the cavitation constraint, this separation metric is scaled by the target tolerance before it is provided to the optimizer. For example, to prescribe $\bar{A}_{\text{sep}} \leqslant 5 \times 10^{-4}$, the constraint is added to the optimization problem as,

$$\frac{\bar{A}_{\text{sep}}}{5 \times 10^{-4}} \leqslant 1. \tag{11}$$

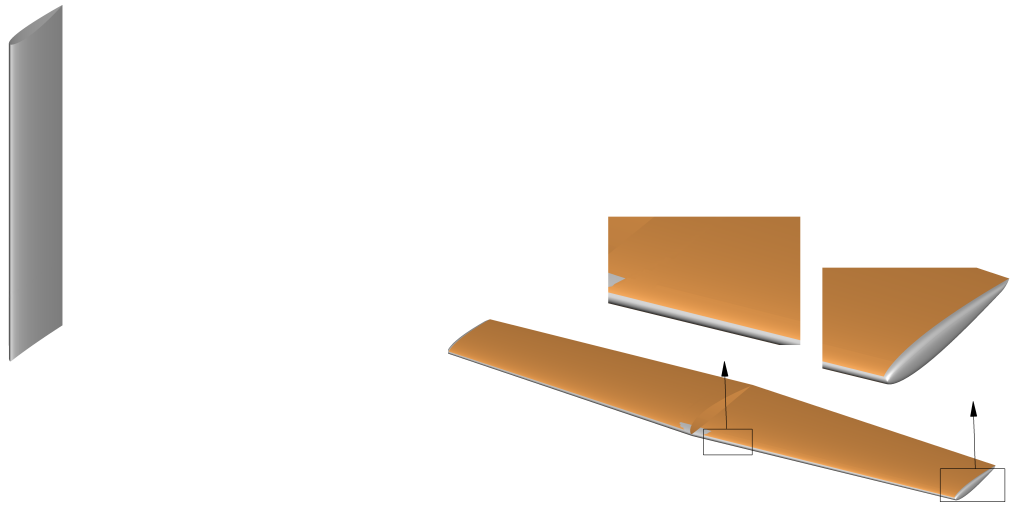

(a) Strut component surface. **(b)** Foil component surface.

Figure 12: Surface groups for the T-foil. The orange surface represents the region where the separation constraint is applied, which excludes the leading edge and the tip.

Table 3: Design conditions and their probabilities of operation (w) with a submergence depth of 0.4 m.

Number	Condition	U_∞	C_L	σ	w
1	Maximum speed	18 m/s	0.2	0.6	15 %
2	Cruise speed	14 m/s	0.3	1.0	60 %
3	Hump speed	11 m/s	0.5	1.5	25 %

3.8 Optimization problem formulation

We consider three flow conditions in the multipoint optimizations, as shown in Table 3. The operating probability of each condition is included in the last column in Table 3.

The optimization problem is summarized in Table 4. For the baseline design, to match the target lift, we first solve an optimization problem with a C_L constraint with respect to a global twist variable, where all sections follow the same change in twists. In subsequent studies, we initialize the optimization problem with all twists set to the corresponding angle, so the lift is matched at the initial point at the cruising condition. We assume that the T-foil operates with the strut vertical. Therefore, we only consider two rake variables at the maximum speed and hump speed conditions to adjust the loading at these design conditions. Cavitation and separation constraints are enforced in each optimization case, while separation constraint is only enforced at the highest C_L condition.

Table 4: T-foil optimization problem description.

		Description	Lower	Upper	Units	Quantity
Minimize	$\sum w_i \times \text{Drag}_i$	Weighted total drag (foil and strut)	–	–	N	1
with respect to	s	Shape (FFD control points)	-0.05	0.05	m	180
		Twist	-10	10	deg	8
	λ	Sweep	0	10	deg	1
	c_{foil}	Foil chords	$0.5c_0$	$1.2c_0$	m	3
	c_{strut}	Strut chord	$0.5c_0$	$1.2c_0$	m	1
	r_{foil}	Foil rake	-5	5	deg	2
	r_{strut}	Strut rake	-5	5	deg	2
	$2b$	Span	$0.9b_0$	$2b_0$	m	1
		Total number of design variables				**198**
subject to		Lift coefficient	0.0	0.0		3
		Fixed leading edge and trailing edge				30
		Monotonic chord constraint				3
	$\bar{A}_{\text{cav}}$	Cavitation constraint	–	2×10^{-5}		3
	$\bar{A}_{\text{sep}}$	Separation constraint	–	5×10^{-4}		1
	t_{2D}	Thickness constraint	$0.6t_0$	–	m	42
	t_{1D}	Trailing edge thickness constraint	t_0	–	m	32
	S	Projected area constraint	$0.985S_0$	$1.015S_0$	m^2	1
		Chord consistency constraint				2
		Junction twist difference constraint				3
		Symmetry shape constraint				84
		Total number of constraints				**204**

3.9 Optimization cases

We set up three different optimization cases to investigate the trade-offs between delaying cavitation, reducing flow separation, and reducing drag. These cases will also help determine how different shape variables affect the flow and drag. When discussing the results, we first introduce the "restricted junction" case and later compare it with the other two cases, "shape-only with restricted junction" and "full optimization" to investigate the influence of the planform variables and a finer junction shape manipulation on design performance. For the "restricted junction" and "shape-only with restricted junction" cases, the shape variables at the junction restrict the top FFD control points from moving up, and the bottom FFD control points only move down to

avoid crossing the top and bottom surfaces. The difference between these two cases is that the "shape-only with restricted junction" does not consider planform variables (chord, span, and sweep variables). Contrary to these two cases with restricted freedom on the junction shape, the "full optimization" case has unrestricted design freedom on the junction shape while also considering planform variables.

4 Results

In Section 4.1, we first show the optimal result from the restricted junction design study and compare this result with the baseline. We discuss how the design considerations of each condition favor different shapes and how the optimizer handles the conflicting requirements and trade-offs. In Section 4.2, we conduct two additional multipoint optimizations to investigate further how planform variables and the detailed junction geometry influence the design. All optimizations converged to an optimality tolerance of less than 9×10^{-4}.

We show the final geometry and the metrics from different conditions for each result. We compare drag coefficient (C_D), pressure coefficient (C_p) contours, separation regions, spanwise lift distributions, and structural performance between the baseline and the optimized designs.

4.1 Hydrodynamic optimization

To better resolve the conflicts between various design conditions and balance the trade-offs, it is necessary to conduct multipoint optimizations because each design condition favors a different shape for performance improvement. For example, if the same lift is maintained at different operating speeds, cavitation is more likely to occur at high-speed (low σ) conditions. At the same time, separation is more likely to occur at high C_L conditions with lower operating speeds. As illustrated in Figure 13, avoiding leading edge cavitation requires a cross-section shape that shifts the loading towards the trailing edge to reduce the suction peak. However, such a load shift can increase the adverse pressure gradient near the trailing edge and thus the likelihood of trailing edge flow separation.

The multipoint optimization here considers all the design conditions listed in Table 3, as well as cavitation and separation constraints at corresponding design conditions. We impose the separation constraint at $C_L = 0.5$ only because flow separation is most likely to occur at the highest C_L or α design condition. Although the baseline violates the separation constraint at $C_L = 0.3$ (as shown later in Figure 15), flow separation is avoided for the optimized design at $C_L = 0.3$ if separation is constrained from occurring at a higher C_L condition.

We first show and discuss the restricted junction optimization case in this section. Figure 14 shows the optimization convergence history of this restricted junction design. We show the planform shapes and the front views of the junction region at selected iterations above the drag history to show how these shapes evolve during the optimization. As shown in Figure 14, this design is driven by the separation constraint at $C_L = 0.5$, and the cavitation constraints at $C_L = 0.2$ and $C_L = 0.5$. As shown in the figure, the optimizer increases the junction thickness and creates a fairing at the junction to prevent a local low-pressure region and thus avoid junction cavitation.

Additionally, the planform variables also help reduce drag and avoid junction cavitation and separation. This multipoint optimization creates a planform that balances the trade-offs between design conditions. The optimized T-foil has a longer span and a shorter tip chord than the baseline to reduce 3-D losses and the lift-induced drag at higher C_L conditions. On the other hand, this design has a longer root chord that helps avoid junction cavitation and separation. First, the longer root chord helps mitigate the junction cavitation by decreasing the local sectional lift coefficient

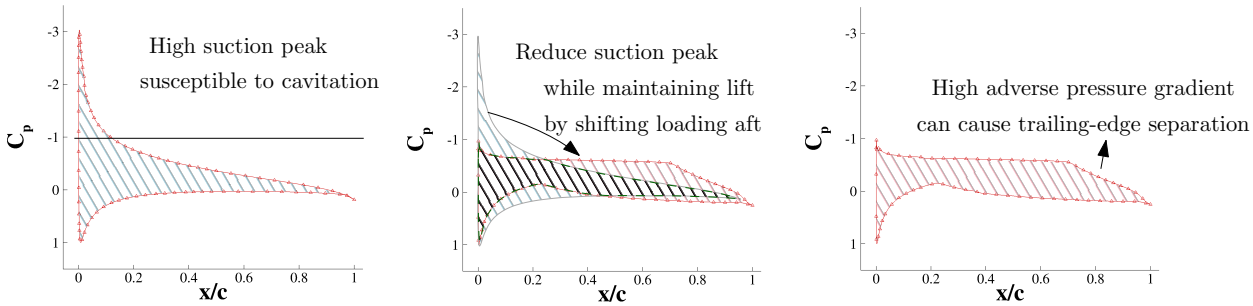

Figure 13: Conflict between avoiding leading-edge cavitation and trailing-edge separation. The blue and red shades represent C_p curves of two different hydrofoils that provide the same 2-D lift. The hydrofoil with blue shaded C_p is susceptible to leading-edge cavitation due to a high suction peak. By shifting the load aft, the hydrofoil with red-shaded C_p avoids leading-edge separation but is prone to trailing edge separation due to a high adverse pressure gradient near the trailing edge.

while maintaining the load. Second, a longer root chord creates enough distance in the streamwise direction to separate the maximum thickness locations of the foil and the strut while keeping enough distance after the maximum thickness to attenuate the adverse pressure gradient. The planform area constraint introduces a conflict between avoiding junction cavitation (increasing the root chord) and reducing lift-induced drag (increasing span). As a result, the span does not increase to its upper limit. Further decreasing the chord length might compromise the friction drag reduction at the $C_L = 0.2$ condition. This is because longer chords reduce the average skin friction and thus result in a lower skin friction drag for the same planform area as explained by Bons et al. [71].

Figure 15 compares the baseline and the restricted junction design in more detail. The yellow-shaded region indicates cavitation inception, whereas the green-shaded region in view A indicates flow separation. Expectedly, the baseline experiences the most severe separation at $C_L = 0.5$, as shown by the largest green-shaded region in Figure 15. Cavitation is a more significant issue at $C_L = 0.2$ because of the lower σ at a higher speed. The surface C_p contours and the streamlines show that the optimized T-foil avoids separation and delays cavitation at all design conditions. The optimizer modifies the cross-sectional geometry to shift the streamwise loading towards the trailing edge to reduce the suction peaks and avoid cavitation.

Although this optimized T-foil significantly delays cavitation compared to the baseline, there remains a cavitation-prone area near the leading edge, as shown by the yellow-shaded region in view B in Figure 15 and by the $-C_p > \sigma$ observed in the sectional pressure plot in the lower portion of Figure 15 for $C_L = 0.2$ at $y/b = 0.5$ and $y/b = 0.9$. This leading-edge pressure side cavitation occurs due to the higher camber and lower twist angle. The cavitation constraint tolerance that we chose allows the design to have this minor leading-edge pressure side cavitation on the outboard at $C_L = 0.2$ when the junction cavitation is completely avoided. If we decrease the cavitation tolerance at $C_L = 0.2$, the small outboard leading-edge region prone to cavitation could be avoided, albeit with a drag penalty. Nevertheless, this cavitation-prone area is minor and the restricted junction optimized T-foil achieves a total weighted drag reduction of 3.9% compared to the baseline over all three design conditions.

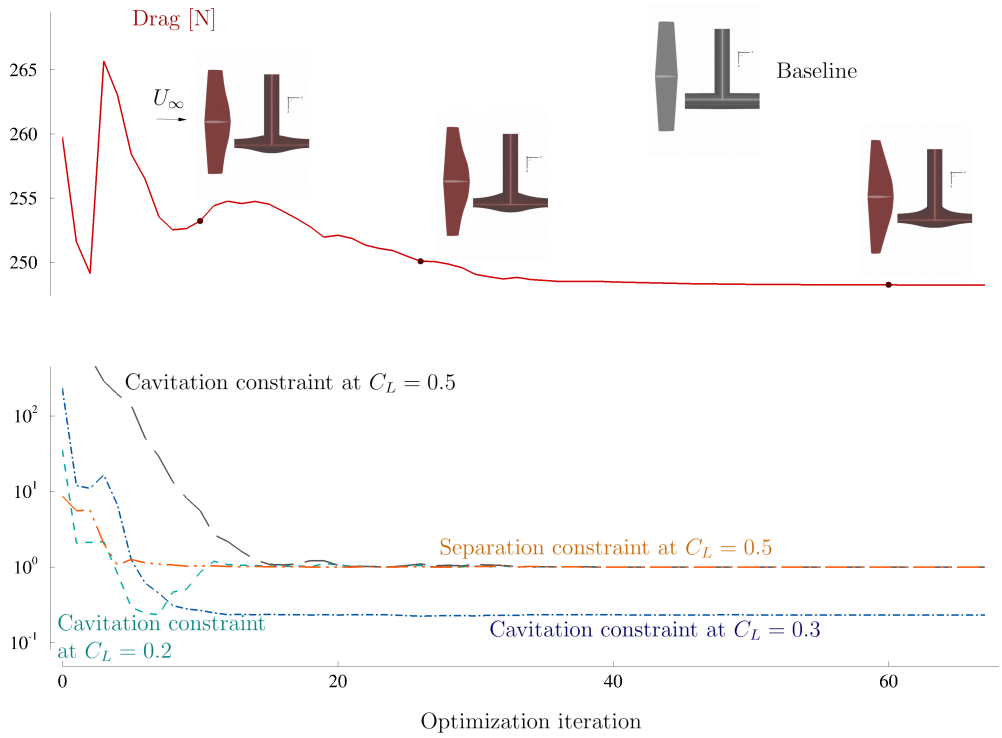

Figure 14: Optimization histories of the restricted junction optimization. The planform shapes and the front view of the junction region of the T-foil at selected iterations are shown above the objective iteration history. The total CPU time for the optimization considering three conditions is 4 days using 240 cores (2.1 GHz Intel Xeon Platinum 8160).

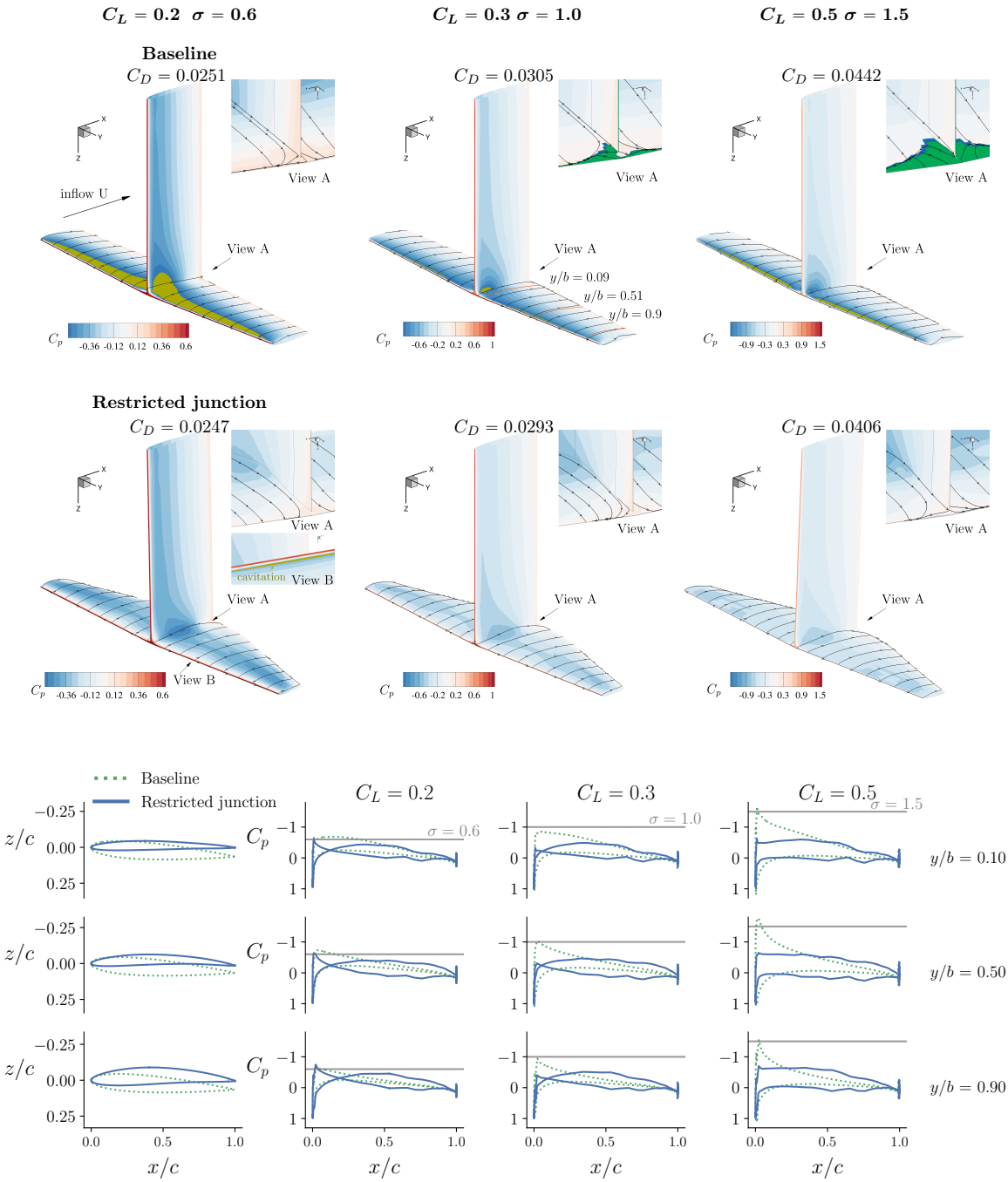

Figure 15: Comparison of surface pressure coefficient contours on the top and cross-sectional shapes and sectional pressure distributions on the bottom for the baseline and the restricted junction multipoint optimized T-foil. The yellow region represents the area that is susceptible to cavitation. The green shade indicates separation. The multipoint optimization with restricted junction reduces the drag by 1.5% ($C_L = 0.2$), 3.8% ($C_L = 0.3$), and 8.1% ($C_L = 0.5$). The restricted junction design flattens the trailing edge near the junction to delay separation at the high C_L condition, as shown by the cross-sectional shape and pressure coefficient curves at $y/b = 0.1$.

4.2 Comparison of different multipoint optimizations

We conduct two additional multipoint optimizations to investigate how the planform variables and more design freedom at the junction benefit the design. The first additional case has the same design variables as the restricted junction optimization, except that it does not consider planform variables. We will refer to this case as "shape-only with restricted junction" or "shape-only" for brevity. The second additional case has more freedom to change the junction shape than the restricted junction optimization shown in the previous subsection. Specifically, the control points along the top and bottom of the junction region can move both up and down without the direction limitation based on their position on the FFD volume, and the foil planform is allowed to change. We will refer to this case as "full optimization". We summarize all the multipoint optimization results in Table 5 and compare the total drag and foil drag reduction weighted by the probability of operation as shown in Table 3. The baseline and the multipoint optimized design geometries are shown in Figure 16. The surface C_p contours and streamlines are compared in Figure 17. Figure 18 compares the sectional shapes and C_p curves. Spanwise normalized lift distributions are shown in Figure 22.

Table 5: Summary of multipoint optimization cases. The drag values are the average drag over the three operating conditions weighted by the probability of operating as shown in Table 3. The planform dimension variables are shown as the ratios relative to the baseline.

	Performance				Planform variables			
Case name	Total drag [N]	Total drag reduction	Foil drag [N]	Foil drag reduction	Span	Root chord	Middle chord	Tip chord
Restricted junction	248	3.9%	149	16.8%	1.03	1.15	0.90	0.58
Shape-only with restricted junction	254	1.6%	175	2.3%	–	–	–	–
Full optimization	242	6.4%	145	18.9%	1.06	1.07	0.92	0.60

The shape-only with restricted junction design has higher total weighted drag than the restricted junction design and the full optimization design because it lacks planform variables and has limited freedom to shape the junction. As shown in Table 5, the substantial difference in drag reduction between the restricted junction and the shape-only designs illustrates the importance of planform variables in the design.

The full optimization design achieves a planform shape similar to that of the restricted junction design because they have similar freedom in planform design variables, as shown in Figure 16. The restricted design has a longer root chord and thicker cross sections near the junction as a result of avoiding junction cavitation, reducing flow separation, and the limited junction shape freedom. To avoid the junction cavitation, the optimizer shifted the maximum thickness location of the foil away from the maximum thickness location of the strut. The junction shape restriction only allows the shift of the maximum foil thickness location by increasing the thickness. Meanwhile, this maximum thickness increase requires a longer distance in the streamwise direction after the maximum thickness location to avoid a high curvature and associated adverse pressure gradient. Consequently, the restricted design has a higher total weighted drag than the full optimization design. The full optimization design achieves about 2.5% higher drag reduction than the restricted junction design (see Table 5).

Figures 17 and 18 compare the cavitation and separation behaviors between cases in more detail. The shape-only design avoids cavitation at the two higher C_L conditions (except for minor leading-edge suction side cavitation at $C_L = 0.5$). However, it is still susceptible to cavitation at the junction at $C_L = 0.2$. Note that this junction cavitation can cause material erosion and increase stress fluctuations of the critical junction, which will accelerate fatigue, and the resultant damage is costly to fix.

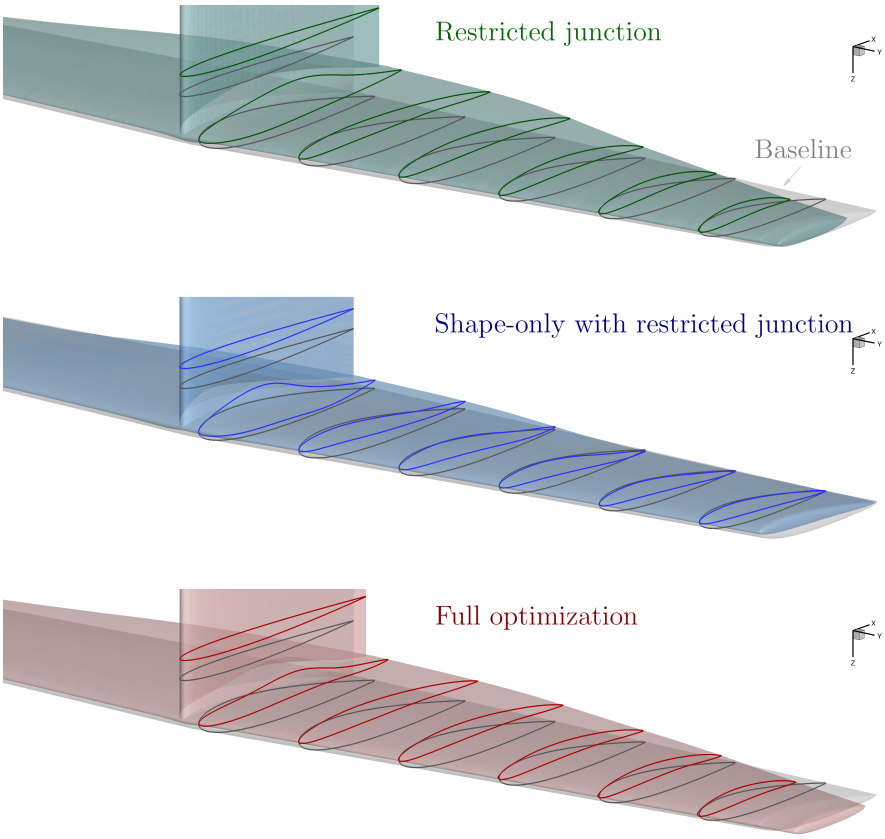

Figure 16: Geometry comparison between multipoint optimization results. The light gray shape is the baseline geometry. Six foil slices are selected to show the cross-sectional shapes along the span. One slice is selected on the strut to show the strut chord change. The selected slices on the strut are at different locations for the baseline and the optimized T-foils to distinguish between the baseline and the optimized hydrofoil strut chord lengths.

The maximum thickness increases close to the junction to create a smooth transition that delays cavitation. However, the distance between the maximum thickness location of the strut and the maximum thickness location of the foil was not enough to avoid junction cavitation altogether. Without chord variables, the shape-only design cannot rely on increasing root chord to help mitigate junction cavitation and separation. The curvature after the maximum thickness point has to decrease significantly to attenuate the adverse pressure gradient and avoid separation due to the thickness increase. The suction and pressure side C_p curves near the trailing edge at the inboard portion ($y/b = 0.1$) almost overlap to avoid separation. The cross-sectional shapes in Figures 16 and 18 also show that the shape-only design has a flat trailing edge along almost the entire span. Without planform variables, satisfying separation constraint requires a near-zero loading near the trailing edge, even at positions away from the junction.

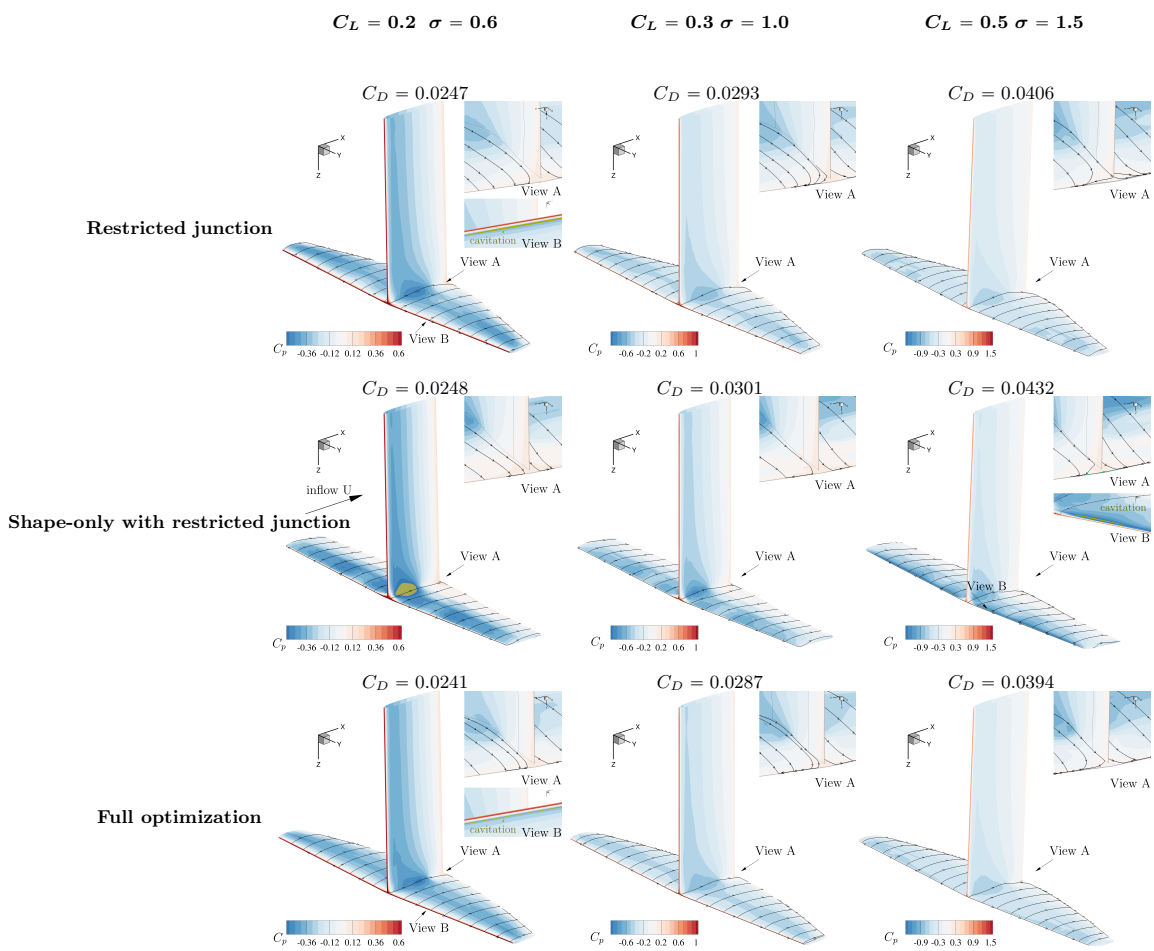

Figure 17: Comparison of surface pressure coefficient contours and streamlines between multipoint optimized T-foils. The yellow region represents the area that is susceptible to cavitation. Separation has been avoided for all the cases shown, and hence no green shaded region is shown in this figure. The shape-only with restricted junction design reduces the drag by 1.1% ($C_L = 0.2$), 1.4% ($C_L = 0.3$) and 2.3% ($C_L = 0.5$) compared to the baseline. The full optimization design provides better overall performance because it has more freedom to shape the junction. The full optimization design reduces the drag by 3.9% ($C_L = 0.2$), 6.3% ($C_L = 0.3$) and 10.9% ($C_L = 0.5$) compared to the baseline.

Unlike the shape-only design, the restricted junction design and the full optimization design do not exhibit zero loading over a significant portion near the trailing edge but can still avoid

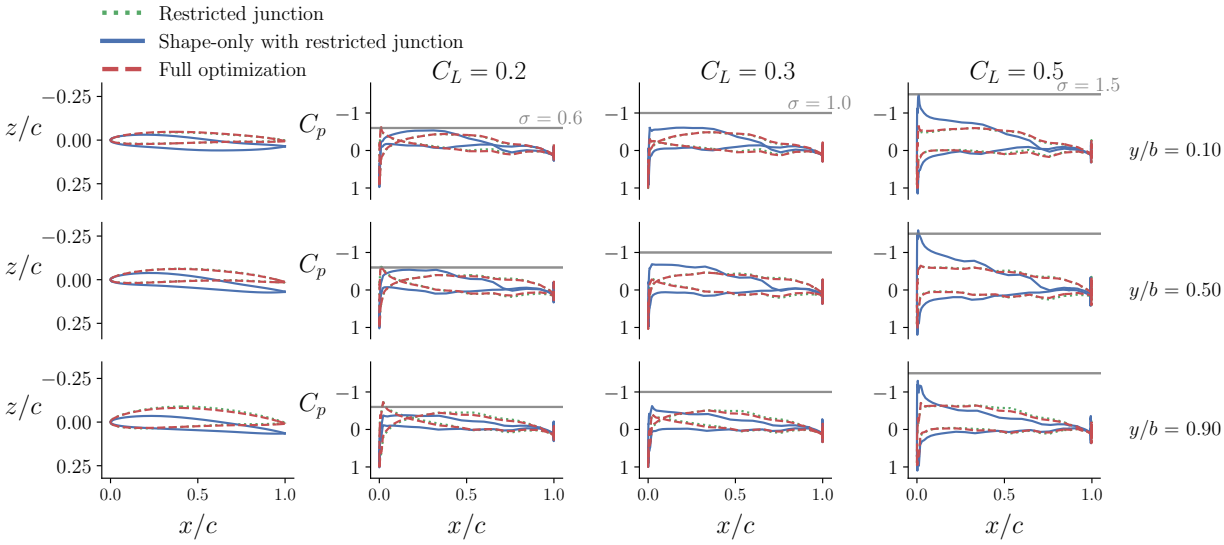

Figure 18: Comparison of cross-sectional shapes between different multipoint optimized T-foils. The full optimization design (red dashed lines) and the restricted junction (green dotted lines) have a higher camber but lower twist across the span compared to the shape-only with restricted junction (solid blue lines) designs. The full optimization design can avoid junction cavitation and trailing edge separation at all three design conditions while reducing more drag. With more freedom at the junction shape, the full optimization design can better utilize junction shape and camber to achieve an optimal load distribution that balances the cavitation and separation requirements at the high C_L condition.

separation. This is attributed to the root chord increase and achieving an optimal camber (shape) at the junction and thus an optimal streamwise pressure gradient and loading distribution. Not having to sustain zero loading near the trailing edge, the restricted junction design and the full optimization design can move more loading aft and achieve a much higher cavitation inception speed. As shown in Figure 18, the full optimization design and the restricted junction have a much lower $-C_{p_{\min}}$ (suction peak) compared to the shape-only design. Allowing the strut planform and cross-sectional geometries to change together helps avoid cavitation at the junction.

By allowing more freedom on the junction shape, the full optimization design can move the maximum foil thickness location and produce ideal curvature after the maximum thickness point without excessively increasing the maximum thickness and the root chord length. As a result, the full optimization design avoids cavitation at the junction for all three C_L conditions while achieving a higher drag reduction. However, it has slight leading-edge pressure side cavitation at outboard sections similar to the restricted design, as indicated by the $-C_p > \sigma$ observed in the red dashed line for $C_L = 0.2$ in Figure 18. Higher design freedom on the junction geometry benefits cavitation performance and separation performance.

To evaluate the cavitation performance over a wider range, we plot cavitation inception speeds versus allowable loading for all three multipoint optimization cases in Figure 19. This type of plot is called a *cavitation bucket*, although the bucket is plotted upside-down. The design can operate cavitation-free under the conditions inside the cavitation bucket, while cavitation occurs outside the bucket. Leading-edge suction side cavitation typically occurs when operating on the right side outside the cavitation bucket. In contrast, leading-edge pressure side cavitation typically occurs when operating on the left side outside the bucket. Mid-chord cavitation is likely to occur when operating on the top outside of the cavitation bucket bottom. The junction cavitation occurrence

might complicate the interpretation of the cavitation mechanism from the cavitation bucket plot.

We run analyses for the optimized T-foils with the nominal inflow velocity and then extract the $C_{p_{\min}}$ from the solution to compute the cavitation inception speed with the formulation:

$$U_{\text{cav}} = \sqrt{\frac{p - p_{\text{vapor}}}{0.5\rho(-C_{p_{\min}})}}, \tag{12}$$

where p is the ambient pressure, p_{vapor} is the saturated vapor pressure, and ρ is the water density. We compute the loading values from the cavitation inception speeds and the corresponding C_L. The tips and the trailing edge were excluded when extracting the $C_{p_{\min}}$ to avoid the artificial extreme values caused by the CFD discretization. As shown in Figure 19, the restricted junction design and the full optimization design have similar cavitation buckets. Both can sustain higher loading than the shape-only design at the same cavitation number. Although all designs are cavitation-free at the cruising point, the safety factor is higher for the restricted junction design and the full optimization design (further inside the bucket boundary), which is preferred because of the higher safety margin at sea. In addition, even though all three designs are susceptible to cavitation at the maximum speed condition, the shape-only design has severe junction cavitation. In contrast, the restricted junction design and the full optimization case only have leading-edge pressure side cavitation in a limited small region. This is also the reason for the difference in the distance from the cavitation bucket boundary. At the highest C_L condition with 25% operating probability, leading-edge suction side cavitation occurs for the shape-only design because of high twist angles; however, this is not a problem for the other two designs.

We focus on the positive lift range, so the optimized T-foils exhibit better performance in the positive loading range. In contrast, the cavitation performance degrades significantly when operating towards zero or negative loading range and becomes even worse than the baseline. Figure 20 shows the sectional C_p curves that correspond to the data shown in Figure 19. A darker line represents the result of a higher angle of attack. At lower α, the three cases have similar C_p ranges, so the difference in cavitation inception speeds is mainly caused by the cavitation at the junction. At high α, the restricted junction and the full optimization designs have higher cavitation inception speeds because of lower suction peaks at the leading edge in the outboard portion than the shape-only design.

To compare the efficiency across a broader range, we plot the C_D versus C_L, as shown in Figure 21. Similar to the observation in Figure 17, the shape-only with restricted junction has the highest drag over nearly the entire positive lift range. The full optimization design has the lowest drag. This is mainly because the full optimization design has optimal lift distribution, reduced thickness near the junction, and shorter root and strut chords.

Next, we compare the spanwise normalized lift, C_l (total sectional lift coefficient), C_d (total sectional drag coefficient), twist, and chord distributions between these multipoint optimizations in Figure 22. The restricted junction and full optimization designs have similar normalized lift distributions; both are closer to the elliptical distribution than the shape-only design. Hence, both optimization cases with planform variables achieve a lower lift-induced drag than the shape-only design. The spanwise normalized lift distribution of the shape-only design is wavy because the requirement of reducing loading near the junction leads to a sudden variation in the loading distribution. Without planform variables and enough freedom to optimize the junction shape, the optimizer has to reduce the loading near the junction to delay cavitation and separation for the shape-only design. From the C_d distribution, the C_d of the restricted junction and full optimization designs are lower than the shape-only design on average.

Despite the similar spanwise lift distributions, the restricted junction design has a slightly lower

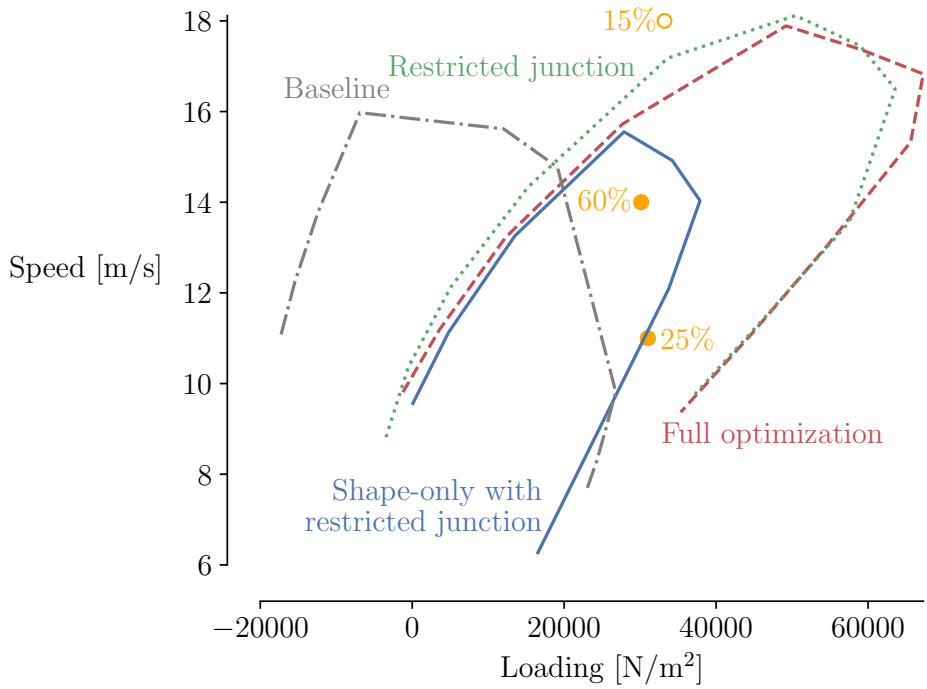

Figure 19: Dimensional cavitation buckets plotted up-side-down for the baseline and the three optimized designs. At a similar cavitation inception speed, the restricted junction design and the full optimization design can carry higher loading than the shape-only design at the design condition range. The orange symbols represent the design conditions. The probability of operation of each design condition is listed next to the corresponding symbol.

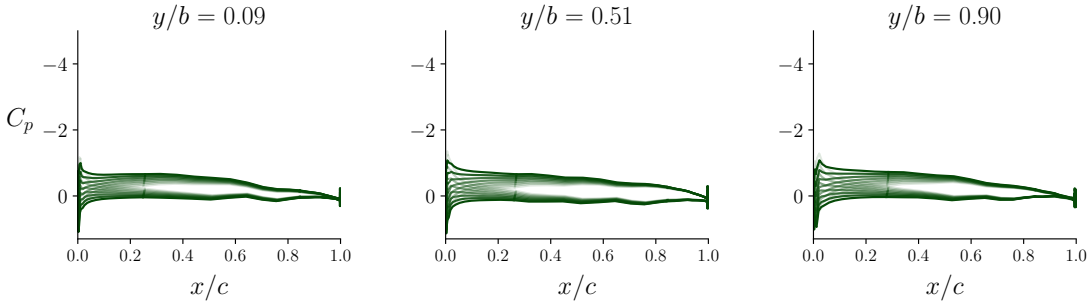

(a) Restricted junction

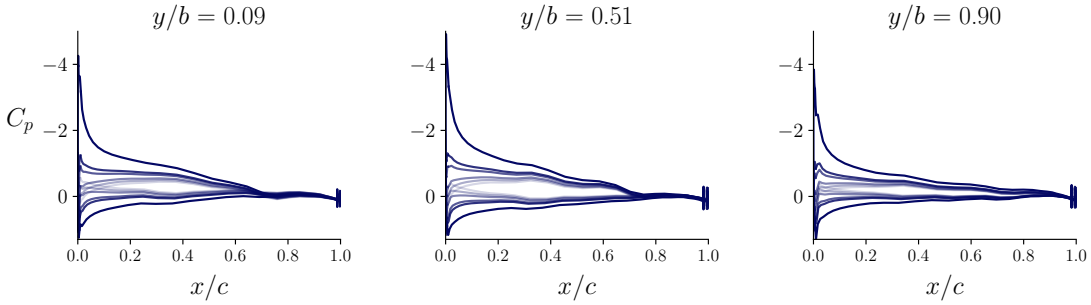

(b) Shape-only with restricted junction

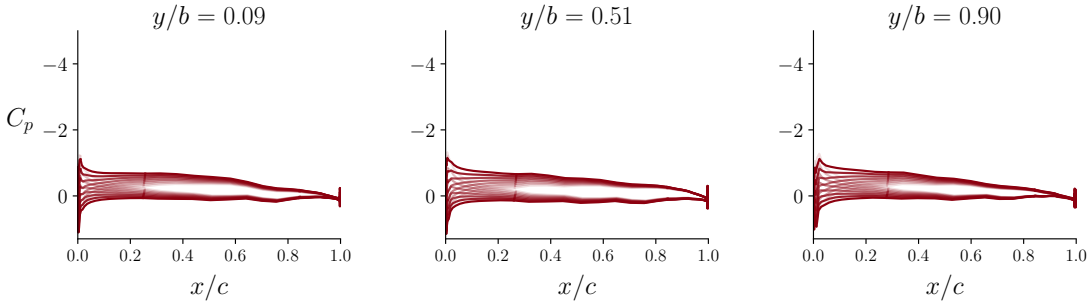

(c) Full optimization

Figure 20: Sectional C_p curves at α values ranging from -4° to 4°. The line darkness increases with α. During the design condition range, the cavitation inception speeds of the restricted junction design are mainly limited by the cavitation at the junction. At high α, the restricted junction design and the full optimization design have lower suction peaks than the shape-only design.

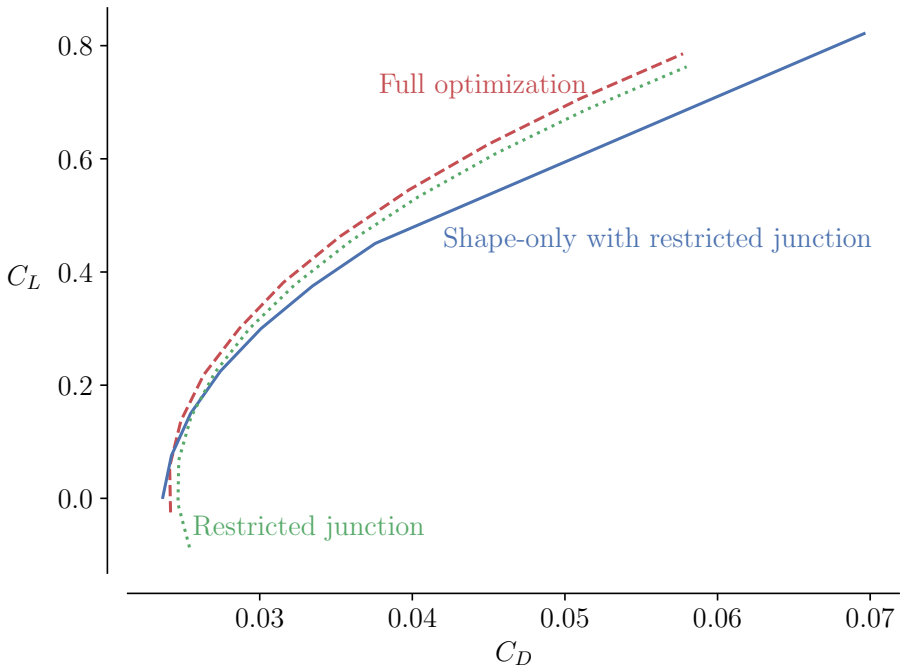

Figure 21: Lift-drag polars for multipoint optimized hydrofoils at the nominal inflow condition with $U = 14$ m/s. The full optimization design has the lowest drag for $C_L \geqslant 0.2$.

C_l near the junction because of a longer root chord. This lower C_l helps mitigate the junction cavitation when the junction shape change is limited.

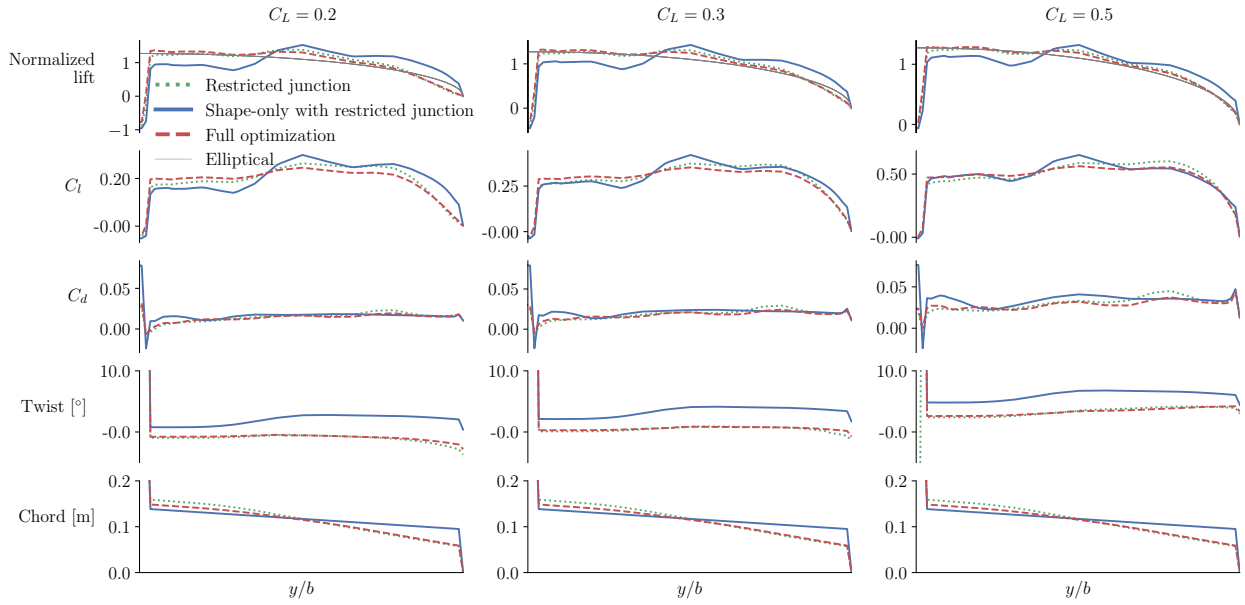

Figure 22: Spanwise normalized lift, C_l (total sectional lift coefficient), C_d (total sectional drag coefficient), twist, and chord distributions of multipoint T-foil optimizations.

4.3 Evaluation with the fine mesh

Because we use the coarse mesh in the optimizations for computational efficiency, we verify the performance improvement of the optimal designs and compare them to the baseline using the fine mesh. Figure 23 compares the cavitation loading buckets and Figure 24 compares the drag polars.

As shown in Figure 23, when evaluating with the fine mesh, the cavitation performance is similar to the results obtained with the coarse mesh. The optimized T-foils have higher cavitation inception speeds in the design condition and a higher lift range than the baseline. On the other hand, the baseline T-foil has higher cavitation inception speeds around zero or negative lift ranges; such a design would not be useful for a foil but useful for a strut. We focus on a positive lift design range in this paper. Hence, the optimized result has a non-symmetrical section for the foil and a cavitation bucket that is skewed towards positive loading. The cross-section of the strut is unmodified except locally near the junction and is symmetrical. However, a design with high cavitation inception speeds around zero lift might be preferred in certain circumstances, such as for rudders and other control surfaces, whose sections and cavitation buckets are typically symmetrical. Eppler and Shen [21] commented that it is difficult to find a hydrofoil section that performs well for all applications. Since each section has its pros and cons, the choice should be based on the actual operating conditions.

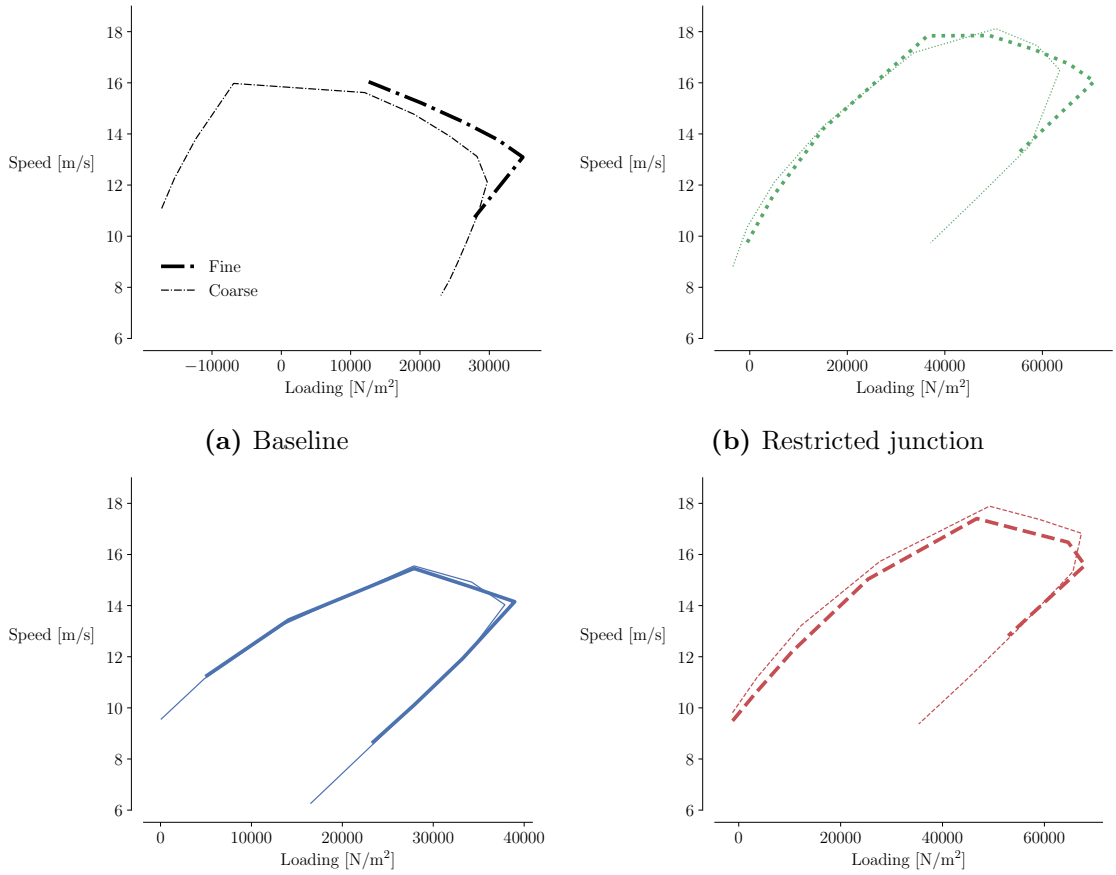

(a) Baseline

(b) Restricted junction

(c) Shape-only with restricted junction

(d) Full optimization

Figure 23: Cavitation bucket comparison between the coarse mesh and the fine mesh of the baseline and the three optimized T-foils. No significant difference is observed between the coarse and fine mesh results for all four T-foils.

The drag polar comparison in Figure 24 shows the lift-drag relation for the fine mesh shown in thick lines follows the same trend as the results from the coarse mesh shown in thin lines for all four T-foils. The drag polar curves of the fine mesh show a constant downward offset from the coarse mesh results for all the cases, confirming that the gradients are similar between the coarse and fine mesh. The optimized T-foils still have lower drag than the baseline for $0.2 \leqslant C_L \leqslant 0.5$ when evaluating the fine mesh.

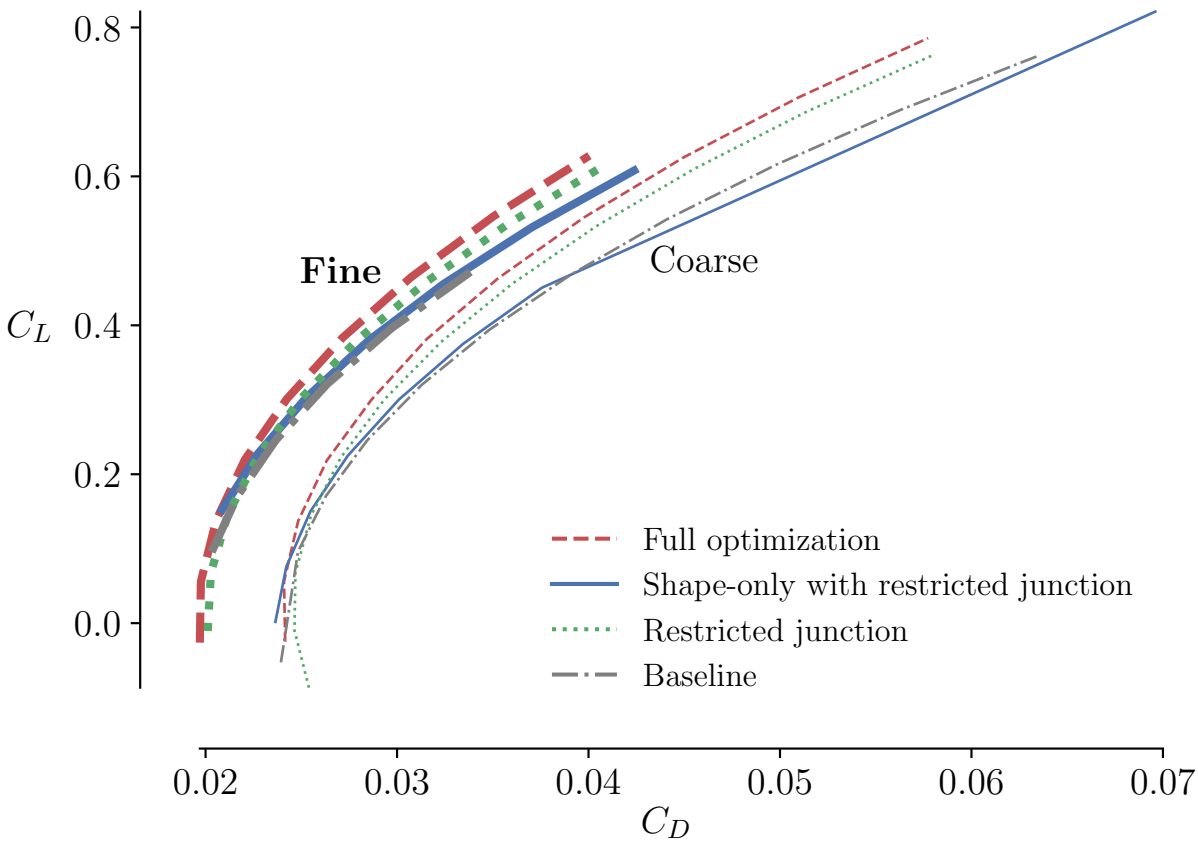

Figure 24: Drag polar comparison between the coarse mesh (thin lines) and the fine mesh (thick lines) for all four T-foils. A similar horizontal shift in drag coefficient is observed for the fine mesh for all four T-foils. The trends of different T-foils are similar between the coarse mesh and fine mesh results.

As shown in Figure 25, all three optimized T-foils can significantly reduce separation compared to the baseline when evaluated with the fine mesh, with the restricted design and the full optimization design showing similarly low suction peaks. The relative performance improvements in drag, separation, and cavitation are maintained between these T-foils obtained using the fine mesh compared to the coarse mesh results, demonstrating the validity of using the coarse mesh in the optimizations.

4.4 Structural performance of the optimized T-foils

Because we only consider hydrodynamic performance in the optimization, we perform hydrostructural analyses of the multipoint optimization results at the nominal cruising condition $C_L = 0.3$ to see how the optimized T-foils perform structurally compared to the baseline. We

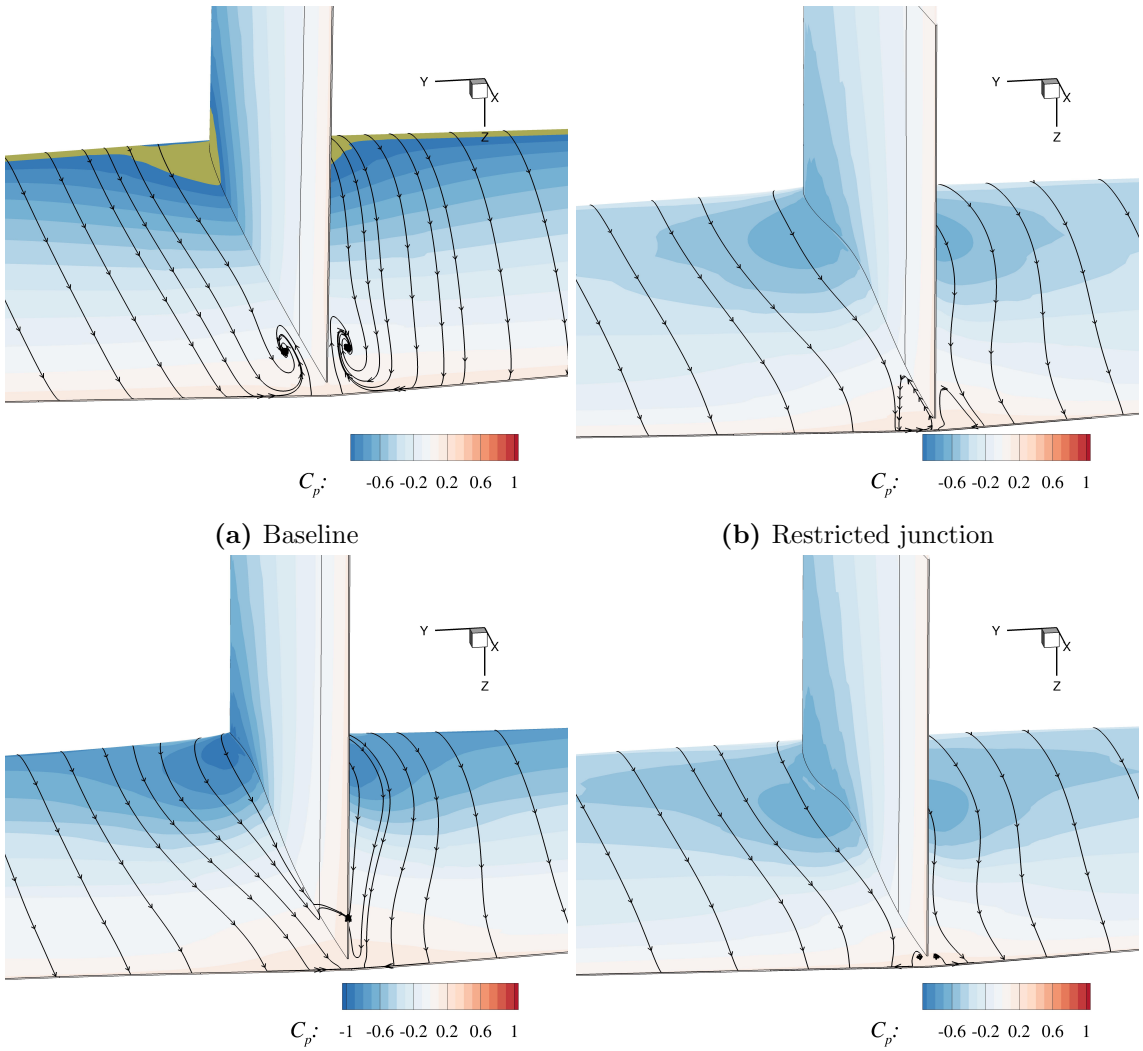

(a) Baseline

(b) Restricted junction

(c) Shape-only with restricted junction

(d) Full optimization

Figure 25: Rear view of the flow streamlines at the junction of the fine mesh analyses at $C_L \approx 0.38$ for all four T-foils. The optimized T-foils still show reduced separation compared to the baseline when being evaluated with the fine mesh. The yellow region represents the area that is susceptible to cavitation, and is only visible for the baseline foil.

extract the geometries from the hydrodynamic optimization results and create structural meshes based on the optimized geometries. The structural material is assumed to be aluminum alloy 6061 for all four T-foils. The properties are listed in Table 6. Figure 26 shows the von Mises contours non-dimensionalized by the material yield strength, f, of the baseline and the optimized T-foils, including both the undeformed and deformed shapes. The maximum failure indicator $f_{\max}$, nondimensional tip deflection δ_{tip}/h, and the tip twist θ_{tip} are listed in the figure captions.

The cross-sectional shape near the $f_{\max}$ position is extracted and shown behind the T-foil as a 2-D blue shape in Figure 26. All optimized T-foils have a higher $f_{\max}$ and higher deformations than the baseline because of the thickness reduction. The restricted junction design and the full optimization design have a nose-down tip twist because their centers of pressure shift towards the trailing edge (as the loading shifts aft because of the change in camber distribution) compared to the shape-only with restricted junction design, as shown in Figure 18. The $f_{\max}$ locations of the optimized T-foils correspond to the minimum thickness location in the cross-sectional shape, as shown in Figure 26.

Although $f_{\max}$ increases for all optimized T-foils, the stress at the junction decreases compared to the baseline because of the resultant junction fairing and the thickness increase at the junction. Since the baseline does not have a fillet at the junction, the high stress could result from the singularity at the sharp corner. The shape-only design has a similar fairing thickness to the restricted junction design at the junction. However, a higher $f_{\max}$ than the restricted junction design because the center of lift moves towards the tip for the shape-only design, leading to a higher bending moment, as shown previously in Figure 22.

As shown in Figure 26, the $f_{\max}$ does not exceed unity, which means that the optimized T-foils are safe with respect to the yield strength (although no safety factor has been applied). However, cyclic loading and load fluctuations are expected for marine structures, and hence, fatigue strength should be used instead of yield strength with the appropriate safety factor. These hydrodynamic-optimized T-foils would not satisfy the fatigue strength requirement if they were constructed with aluminum alloy 6061. Additionally, the higher δ_{tip} of the optimized T-foils suggests accelerated fatigue compared to the baseline because excessive tip deformation can lead to severe flow-induced vibration and dynamic load amplification issues. Hence, hydrostructural optimization is recommended for future designs.

Table 6: Aluminum 6061 material properties

Symbol	Description	Value	Units
ρ_{al}	Solid density	2700	kg/m^3
E	Young's modulus	69	GPa
ν	Poisson's ratio	0.33	–
σ_{yield}	Yield strength	276	MPa

In addition to the static hydrostructural analyses, we analyze the structural (in-air) modes of the baseline and the multipoint optimized T-foils to assess their dynamic performance. Figure 27 compares the first four modes of the baseline and the multipoint optimized T-foils. The mode shapes of the T-foils are governed by the basic configuration, so these four mode shapes are similar between the T-foils. The strut governs the first three modes, so the in-air natural frequencies of these three modes do not vary significantly between the baseline and the optimized T-foils. The first mode of all the optimized T-foils has a slightly higher natural frequency than the baseline because of the increased strut bending stiffness due to a longer strut chord and a decreased moment of

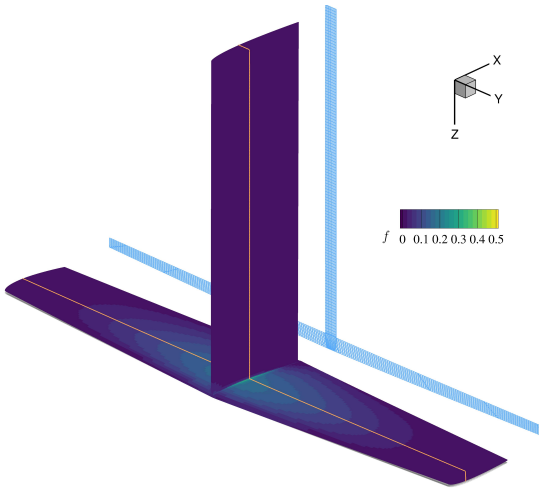

(a) Baseline
$f_{\max} = 0.37$
$\delta_{\text{tip}}/h = 0.01$
$\theta_{\text{tip}} = 0.06^\circ$

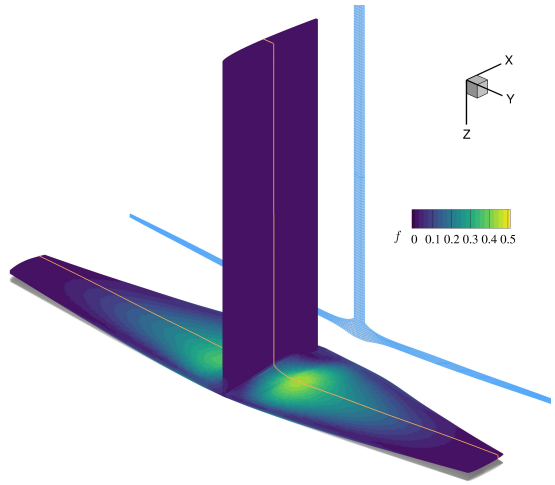

(b) Restricted junction
$f_{\max} = 0.45$
$\delta_{\text{tip}}/h = 0.025$
$\theta_{\text{tip}} = -0.24^\circ$

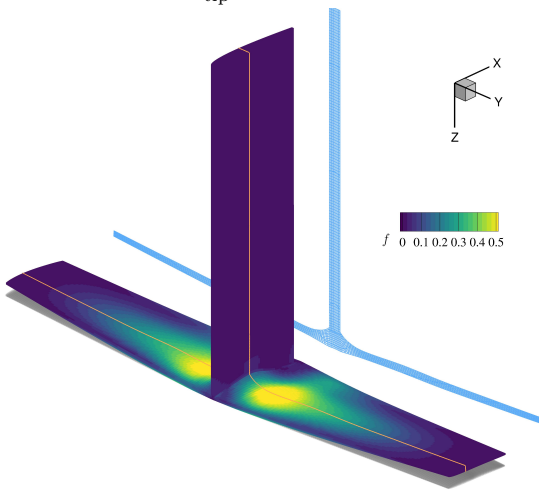

(c) Shape-only with restricted junction
$f_{\max} = 0.62$
$\delta_{\text{tip}}/h = 0.035$
$\theta_{\text{tip}} = 0.15^\circ$

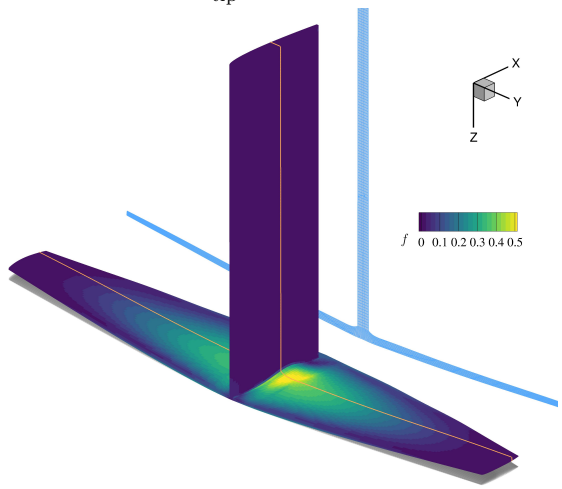

(d) Full optimization
$f_{\max} = 0.54$
$\delta_{\text{tip}}/h = 0.031$
$\theta_{\text{tip}} = -0.26^\circ$

Figure 26: Nondimensional von Mises stress (based on yield strength) contour comparison between the baseline and the multipoint optimized T-foils at nominal $C_L = 0.3$ condition. The undeformed shape is shown in gray. The optimized hydrofoils have higher stresses slightly away from the vertical mid-plane because of the resultant fillet at the junction and the corresponding reduced thickness away from the junction. This thickness reduction can be observed in the chordwise slice projection along the orange line and shown behind the T-foil in light blue shape. Despite this higher maximum stress, the optimized hydrofoil has a less stress concentration at the junction because of the increased thickness and smoother transition at the junction, which reduces the singularity effect.

inertia relative to the strut root due to a foil mass reduction. Similarly, the second modes of the optimized T-foils have higher natural frequencies than the baseline. The third modes are x-axis rotation modes about the junction. The third mode in-air natural frequencies of the optimized T-foils remain approximately the same as the baseline because the relative change of the stiffness and moment of inertia is small. The difference is more prominent for higher modes determined by the horizontal foil, such as the fourth mode. The optimized T-foils have much lower natural frequencies than the baseline because of the reduced foil thickness. The smaller gaps between the frequencies of the higher-order modes of the optimized T-foils may make the optimized T-foils more susceptible to frequency coalescence in water.

This in-water mode coalescence is more likely to occur between the second and the third mode because the motion-dependent added mass effect causes a more significant reduction in the bending-dominated third modal frequencies than in the twisting-dominated second modal frequencies, further decreasing the gap. This modal frequency coalescence can lead to significant dynamic load amplification, damping ratio reduction, and flow-induced vibrations, eventually resulting in accelerated fatigue and other types of structural failures [12, 75, 76]. The potential frequency coalescence and the corresponding impacts highlight the need for the dynamic hydrostructural performance assessment in water to avoid modal coalescence and flutter [77, 78].

In this paper, we develop methods to optimize hydrodynamic lifting surfaces, including junction shape variables, foil cross-section, and planform variables. This is the first step toward designing more complex hydrodynamic configurations. We conduct hydrodynamic optimizations of a canonical T-shaped hydrofoil-strut system with RANS simulations and consider many design variables (198) with constraints limiting cavitation and separation. This T-shaped hydrofoil-strut system consists of a vertical strut and a horizontal foil, both contributing to the total drag of the system.

We performed three multipoint optimizations to investigate how the planform shape and the junction shape impact the performance. We showed the importance of considering many design shape variables, including junction shape. We also investigated the trade-offs between delaying cavitation and separation and reducing drag at high speed and high lift conditions. In the first case, we consider planform variables but limit the freedom of the junction shape change. The second case has no planform variables, and the junction shape change is also limited. In the third case, planform variables and junction geometry change freely (called full optimization design). All multipoint optimizations created a fairing and moved the maximum foil thickness location away from the maximum strut thickness location to delay junction cavitation and modified the foil cross-section geometry to delay separation.

With planform variables, the restricted junction design and the full optimization design can increase the root chord length to help remove junction cavitation at $C_L = 0.2$ and avoid separation at a higher C_L by adjusting the maximum thickness location while maintaining enough distance for a low curvature after the maximum foil thickness location.

With more freedom on the junction shape design, the full optimization design can move the maximum foil thickness location relative to the maximum strut thickness location without excessively increasing the thickness near the junction, and hence it does not need to increase the root chord as much as the restricted junction design to keep the curvature after the maximum thickness point low enough. The full optimization achieves the largest drag reduction among the multipoint optimizations and delays cavitation and separation most effectively. Compared to the baseline, the full optimization design achieves a total drag reduction of 6.4% and a foil drag reduction of 18.9%. The total drag reduction is lower than the foil drag reduction because the current setup did not include strut planform variables. The optimization leads to a longer strut chord and higher strut drag.

Because we mainly optimize the shape of the horizontal foil and the junction, the strut geometry

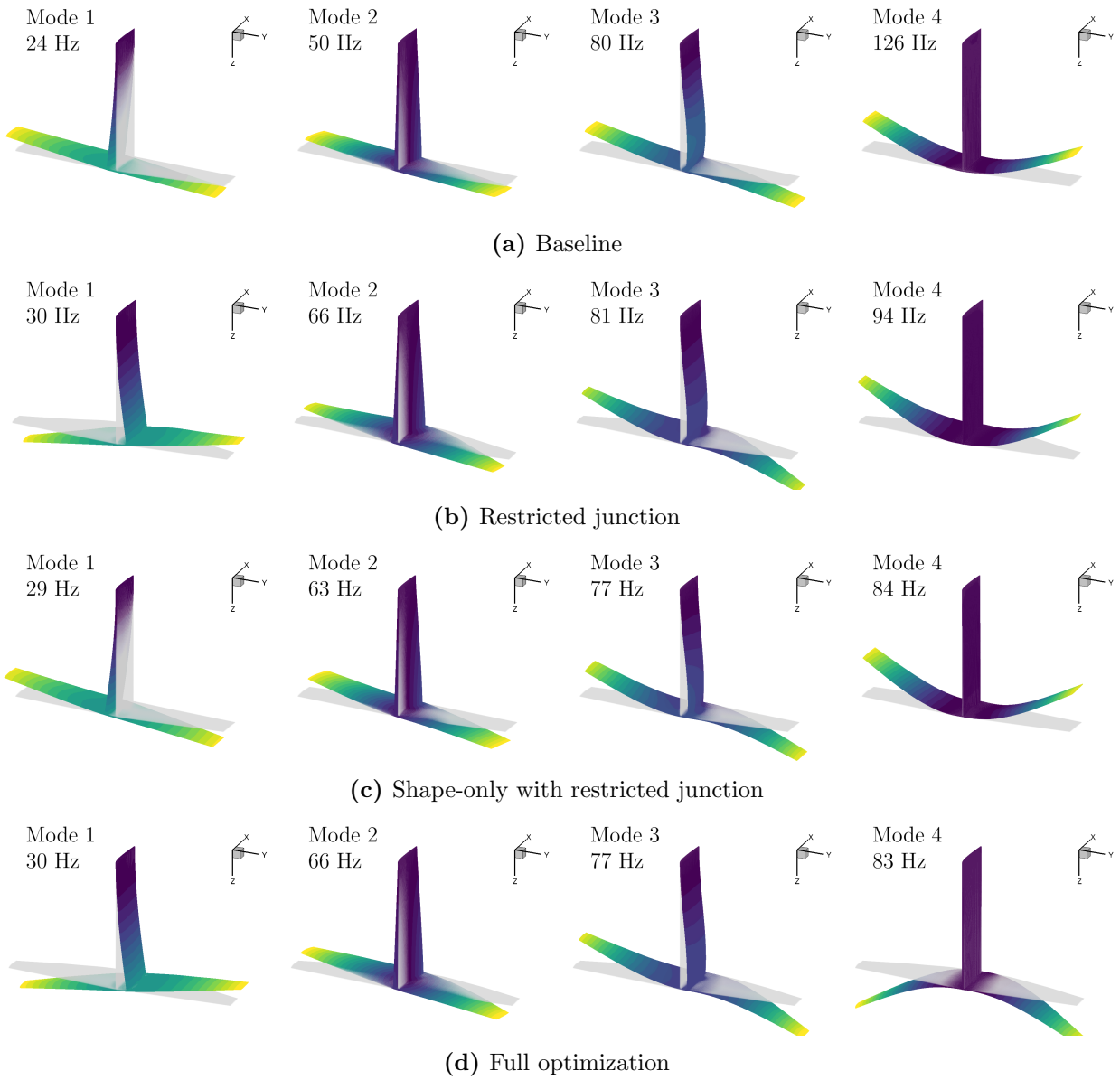

Figure 27: Comparison of first four mode shapes and modal frequencies between the baseline and the multipoint optimized T-foil designs at $C_L = 0.3$. These mode shapes are governed by the basic configuration, so the first four mode shapes of the optimized T-foils are similar to the baseline one. The first three modes are governed by the strut, so the in-air natural frequencies of these three modes do not vary significantly between the baseline and the optimized T-foils. For higher modes where the horizontal foil governs, such as the fourth mode, the difference is more prominent. Due to the reduced thickness, the fourth modes of the optimized T-foils have much lower in-air natural frequencies than the baseline. The smaller gap between the frequencies of the higher modes of the optimized T-foils might cause the optimized T-foils to be more susceptible to frequency coalescence in water.

is not optimal. Further drag reduction and cavitation delay could be achieved by allowing more strut geometric variables to change, such as the cross-sectional shape and chord variations along the strut span. The comparison between these three multipoint optimizations shows that the junction shape, the foil shape, and planform variables can significantly improve the performance. These three optimization cases also demonstrate the importance of the relative position between the maximum foil thickness and the maximum strut thickness in avoiding junction cavitation. This suggests that the relative translation of the foil and the strut is a critical design variable for such a T-foil design.

Analyzing the optimized results obtained using a coarse mesh, using a finer mesh shows that the cavitation performance is similar between the two levels of meshes. Additionally, the drag polars predicted by the coarse mesh followed similar trends to those obtained with the fine mesh, demonstrating that the coarse mesh can be used in gradient-based optimization of the T-foil, including junction shape variables, to minimize CPU time requirements.

Hydrostructural analyses show that these hydrodynamic-optimized T-foils can experience higher deformation and possibly accelerated fatigue failure due to higher flow-induced deformation and vibrations. This highlights the need to consider hydrostructural responses for these T-foil designs. Additionally, the modal analysis results suggest that the optimized T-foils might be susceptible to dynamic load amplifications and even instabilities caused by frequency coalescence of the higher-order modes in water. This is because the reduced foil thickness significantly decreases the frequency gaps between the higher-order modes with low damping. This modal analysis comparison suggests that dynamic response prediction in water can be critical for these designs.

The optimization studies and discussions help us understand the physics of a T-shaped hydrofoil-strut system and provide valuable insights for designers for general hydrodynamic lifting surfaces. The developed methodology is useful for designing next-generation complex hydrodynamic lifting surface systems.

5 Acknowledgments

The work in this paper is supported by US Office of Naval Research, Contracts N00014–16–1–2972 and N00014–18–1–2333 managed by Ms. Kelly Cooper. Part of the computations was performed on the Great Lakes HPC cluster at the University of Michigan Center of Advanced Computing. This work also used the Extreme Science and Engineering Discovery Environment (XSEDE), which is supported by the National Science Foundation grant number ACI1548562 through allocation TG-DDM140001.

References

[1] Brennen, C. E. (ed.), *Cavitation and bubble dynamics*, Cambridge University Press, 2014.

[2] Franc, J.-P., "Physics and Control of Cavitation," *Design and Analysis of High Speed Pumps*, 2006, pp. 1–36.

[3] Jahangir, S., Ghahramani, E., Neuhauser, M., Bourgeois, S., Bensow, R. E., and Poelma, C., "Experimental investigation of cavitation-induced erosion around a surface-mounted bluff body," *Wear*, 2021, p. 203917. https://doi.org/10.1016/j.wear.2021.203917.

[4] Yamatogi, T., Murayama, H., Uzawa, K., Kageyama, K., and Watanabe, N., "Study on Cavitation Erosion of Composite Materials for Marine Propeller," *The 17th International Conference on Composites (ICCM-17)*, Edinburgh, UK, 2009.

[5] Young, Y. L., "Hydroelastic Response of Lifting Bodies in Separated Flows," *NATO-AVT-307: Symposium on Separated Flow: Prediction, Measurement and Assessment for Air and Sea*, Trondheim, Norway, 2019.

[6] Breslin, J. P., and Skalak, R., "NASA Technical Reports Server (NTRS)," Tech. Rep. C-476 NASA-MEMO-2-23-59W, April 1959. URL https://ntrs.nasa.gov/citations/19980228299.

[7] Hecker, R., "Flow separation, reattachment, and ventilation of foils with sharp leading edge at low Reynolds number," *Naval Ship Research and Development Center, Ship Performance Department, Research and Development Report No. 4390, Bethesda, Md 20034, USA*, 1974. URL https://repository.tudelft.nl/islandora/object/uuid%3A731f5618-d83e-4a4a-b37a-09d97f364572.

[8] Harwood, C. M., Young, Y. L., and Ceccio, S. L., "Ventilated cavities on a surface-piercing hydrofoil at moderate Froude numbers: cavity formation, elimination and stability," *Journal of Fluid Mechanics*, Vol. 800, 2016, pp. 5–56. https://doi.org/10.1017/jfm.2016.373.

[9] Young, Y. L., Motley, M. R., Barber, R., Chae, E. J., and Garg, N., "Adaptive Composite Marine Propulsors and Turbines: Progress and Challenges," *Applied Mechanics Reviews*, Vol. 68, No. 6, 2016, p. 060803. https://doi.org/10.1115/1.4034659.

[10] Young, Y. L., Harwood, C. M., Montero, M. F., Ward, J. C., and Ceccio, S. L., "Ventilation of Lifting Bodies: Review of the Physics and Discussion of Scaling Effects," *Applied Mechanics Reviews*, Vol. 69, No. 1, 2017, p. 010801.

[11] Harwood, C. M., Felli, M., Falchi, M., Ceccio, S. L., and Young, Y. L., "The hydroelastic response of a surface-piercing hydrofoil in multi-phase flows. Part 1. Passive hydroelasticity," *Journal of Fluid Mechanics*, Vol. 881, 2019, pp. 313–364. https://doi.org/10.1017/jfm.2019.691.

[12] Harwood, C. M., Felli, M., Falchi, M., Garg, N., Ceccio, S. L., and Young, Y. L., "The hydroelastic response of a surface-piercing hydrofoil in multiphase flows. Part 2. Modal parameters and generalized fluid forces," *Journal of Fluid Mechanics*, Vol. 884, 2019. https://doi.org/10.1017/jfm.2019.871.

[13] Damley-Strnad, A., Harwood, C. M., and Young, Y. L., "Hydrodynamic Performance and Hysteresis Response of Hydrofoils in Ventilated Flows," *Sixth International Symposium on Marine Propulsors*, Rome, Italy, 2019.

[14] Smith, S. M., Venning, J. A., Pearce, B. W., Young, Y. L., and Brandner, P. A., "The influence of fluid–structure interaction on cloud cavitation about a stiff hydrofoil. Part 1." *Journal of Fluid Mechanics*, Vol. 896, 2020, p. A1. https://doi.org/10.1017/jfm.2020.321.

[15] Smith, S. M., Venning, J. A., Pearce, B. W., Young, Y. L., and Brandner, P. A., "The influence of fluid–structure interaction on cloud cavitation about a flexible hydrofoil. Part 2." *Journal of Fluid Mechanics*, Vol. 897, 2020, p. A28. https://doi.org/10.1017/jfm.2020.323.

[16] Young, Y. L., Chang, J., Smith, S. M., Venning, J. A., Pearce, B. W., and Brandner, P. A., "The influence of fluid-structure interaction on cloud cavitation about a stiff hydrofoil. Part 3," *Journal of Fluid Mechanics*, 2021.

[17] Simpson, R. L., "Junction Flows," *Annual Review of Fluid Mechanics*, 2001. https://doi.org/0066-4189/01/0115-0415.

[18] Carlton, J., *Marine Propellers and Propulsion*, Butterworth-Heinemann, 2018.

[19] Drela, M., "XFOIL: An Analysis and Design System for Low Reynolds Number Airfoils," *Low Reynolds Number Aerodynamics*, edited by T. J. Mueller, Springer Berlin Heidelberg, Berlin, Heidelberg, 1989, pp. 1–12. https://doi.org/10.1007/978-3-642-84010-4_1.

[20] Shen, Y. T., and Eppler, R., "Wing Sections for Hydrofoils - Part 2: Nonsymmetrical Profiles," *Journal of Ship Research*, Vol. 25, No. 3, 1981, pp. 191–200.

[21] Eppler, R., and Shen, Y. T., "Wing Sections for Hydrofoils–Part 1: Symmetrical Profiles," *Journal of Ship Research*, Vol. 23, No. 3, 1979, pp. 209–217.

[22] Sacher, M., Durand, M., Berrini, É., Hauville, F., Duvigneau, R., Le Maître, O., and Astolfi, J.-A., "Flexible hydrofoil optimization for the 35th America's Cup with constrained EGO method," *Ocean Engineering*, Vol. 157, 2018, pp. 62–72. https://doi.org/10.1016/j.oceaneng.2018.03.047.

[23] Mishima, S., and Kinnas, S. A., "Application of a Numerical Optimization Technique to the Design of Cavitating Propellers in Nonuniform Flow," *Journal of Ship Research*, Vol. 41, No. 2, 1997, pp. 93–107.

[24] Mishima, S., "Design of cavitating propeller blades in non-uniform flow by numerical optimization," Ph.D. thesis, Massachusetts Institute of Technology. Dept. of Ocean Engineering, 1996.

[25] Kinnas, S. A., "Supercavitating 3-D Hydrofoils and Propellers: Prediction of Performance and Design," Tech. Rep. ADP012091, February 2001.

[26] Young, Y. L., and Kinnas, S. A., "Analysis of supercavitating and surface-piercing propeller flows via BEM," *Computational Mechanics*, Vol. 32, No. 4-6, 2003, pp. 269–280. https://doi.org/10.1007/s00466-003-0484-6.

[27] Young, Y. L., "Fluid–structure interaction analysis of flexible composite marine propellers," *Journal of Fluids and Structures*, Vol. 24, No. 6, 2008, pp. 799–818. https://doi.org/10.1016/j.jfluidstructs.2007.12.010.

[28] Young, Y., "Time-dependent hydroelastic analysis of cavitating propulsors," *Journal of Fluids and Structures*, Vol. 23, No. 2, 2007, pp. 269–295. https://doi.org/10.1016/j.jfluidstructs.2006.09.003.

[29] Li, D.-Q., Grekula, M., and Lindell, P., "A modified SST k-ω Turbulence Model to Predict the Steady and Unsteady Sheet Cavitation on 2D and 3D Hydrofoils," *Proceedings of the 7th International Symposium on Cavitation*, Ann Arbor, Michigan, USA, 2009.

[30] ru Li, Z., and van Terwisga, T., "On the Capability of Multiphase RANS Codes to Predict Cavitation Erosion," *Second International Symposium on Marine Propulsors*, Hamburg, Germany, 2011.

[31] Ji, B., Luo, X., Arndt, R. E., Peng, X., and Wu, Y., "Large Eddy Simulation and theoretical investigations of the transient cavitating vortical flow structure around a NACA66 hydrofoil," *International Journal of Multiphase Flow*, Vol. 68, 2015, pp. 121 – 134. https://doi.org/10.1016/j.ijmultiphaseflow.2014.10.008.

[32] Garg, N., Kenway, G. K. W., Martins, J. R. R. A., and Young, Y. L., "High-fidelity Multipoint Hydrostructural Optimization of a 3-D Hydrofoil," *Journal of Fluids and Structures*, Vol. 71, 2017, pp. 15–39. https://doi.org/10.1016/j.jfluidstructs.2017.02.001.

[33] Garg, N., Pearce, B. W., Brandner, P. A., Phillips, A. W., Martins, J. R. R. A., and Young, Y. L., "Experimental Investigation of a Hydrofoil Designed via Hydrostructural Optimization," *Journal of Fluids and Structures*, Vol. 84, 2019, pp. 243–262. https://doi.org/10.1016/j.jfluidstructs.2018.10.010.

[34] Garg, N., Kenway, G. K. W., Lyu, Z., Martins, J. R. R. A., and Young, Y. L., "High-fidelity Hydrodynamic Shape Optimization of a 3-D Hydrofoil," *Journal of Ship Research*, Vol. 59, No. 4, 2015, pp. 209–226. https://doi.org/10.5957/JOSR.59.4.150046.

[35] Secco, N. R., Jasa, J. P., Kenway, G. K. W., and Martins, J. R. R. A., "Component-based Geometry Manipulation for Aerodynamic Shape Optimization with Overset Meshes," *AIAA Journal*, Vol. 56, No. 9, 2018, pp. 3667–3679. https://doi.org/10.2514/1.J056550.

[36] Liao, Y., Martins, J. R. R. A., and Young, Y. L., "3-D High-Fidelity Hydrostructural Optimization of Cavitation-Free Composite Lifting Surfaces," *Composite Structures*, Vol. 268, 2021, p. 113937. https://doi.org/10.1016/j.compstruct.2021.113937.

[37] Volpi, S., Diez, M., and Stern, F., *Multidisciplinary Design Optimization of a 3D Composite Hydrofoil via Variable Accuracy Architecture*, American Institute of Aeronautics and Astronautics, 2018. https://doi.org/doi:10.2514/6.2018-4173.

[38] Lyu, Z., and Martins, J. R. R. A., "Aerodynamic Design Optimization Studies of a Blended-Wing-Body Aircraft," *Journal of Aircraft*, Vol. 51, No. 5, 2014, pp. 1604–1617. https://doi.org/10.2514/1.C032491.

[39] Mader, C. A., Kenway, G. K. W., Yildirim, A., and Martins, J. R. R. A., "ADflow: An open-source computational fluid dynamics solver for aerodynamic and multidisciplinary optimization," *Journal of Aerospace Information Systems*, Vol. 17, No. 9, 2020, pp. 508–527. https://doi.org/10.2514/1.I010796.

[40] Kenway, G. K. W., Mader, C. A., He, P., and Martins, J. R. R. A., "Effective Adjoint Approaches for Computational Fluid Dynamics," *Progress in Aerospace Sciences*, Vol. 110, 2019, p. 100542. https://doi.org/10.1016/j.paerosci.2019.05.002.

[41] Martins, J. R. R. A., and Ning, A., *Engineering Design Optimization*, Cambridge University Press, 2021. https://doi.org/10.1017/9781108980647, URL https://mdobook.github.io.

[42] Kenway, G. K. W., Secco, N., Martins, J. R. R. A., Mishra, A., and Duraisamy, K., "An Efficient Parallel Overset Method for Aerodynamic Shape Optimization," *Proceedings of the 58th AIAA/ASCE/AHS/ASC Structures, Structural Dynamics, and Materials Conference, AIAA SciTech Forum*, Grapevine, TX, 2017. https://doi.org/10.2514/6.2017-0357.

[43] Yildirim, A., Mader, C. A., and Martins, J. R. R. A., "A Surface Mesh Deformation Method Near Component Intersections for High-Fidelity Design Optimization," *Engineering with Computers*, 2021. https://doi.org/10.1007/s00366-020-01247-w.

[44] Secco, N. R., and Martins, J. R. R. A., "RANS-based Aerodynamic Shape Optimization of a Strut-braced Wing with Overset Meshes," *Journal of Aircraft*, Vol. 56, No. 1, 2019, pp. 217–227. https://doi.org/10.2514/1.C034934.

[45] Acosta, A. J., "Hydrofoils and Hydrofoil Craft," *Annual Review of Fluid Mechanics*, 1973. https://doi.org/10.1146/annurev.fl.05.010173.001113.

[46] Faltinsen, O. M., *Hydrodynamics of high-speed marine vehicles*, Cambridge University Press, 2006. https://doi.org/10.1017/CBO9780511546068.

[47] International Sailing Federation, "IMCA Rules (ISAF approved) – 1st May 2017," , May 2017. URL http://www.moth-sailing.org/wp-content/uploads/2017/05/MTH2017CR010517.pdf.

[48] Royal New Zealand Yacht Squadron, "AC75 Class Rule," , November 2021. URL https://drive.google.com/drive/u/0/folders/1o1BMm3RBb56C0nZPGOcadTE4AXW5dFgp.

[49] America's Cup, "THE TECHNOLOGY," , ???? URL https://www.americascup.com/the-technology.

[50] Giron-Sierra, J., Esteban, S., De Andres, B., Diaz, J., and Riola, J., "Experimental Study of Controlled Flaps and T-Foil for Comfort Improvement of a Fast Ferry," *IFAC Proceedings Volumes*, Vol. 34, No. 7, 2001, pp. 261–266. https://doi.org/10.1016/s1474-6670(17)35093-0.

[51] Scherer, J. O., and Auslaender, J., "Experimental and theoretical performance of a supercavitating hydrofoil operating near a free surface," *Journal of Aircraft*, Vol. 2, No. 2, 1965, pp. 144–152. https://doi.org/10.2514/3.43631.

[52] Binns, J. R., Brandner, P. A., and Plouhinec, J., "The effect of heel angle and free-surface proximity on the performance and strut wake of a moth sailing dinghy rudder T-foil," Auckland, NZ, 2008. URL https://eprints.utas.edu.au/8987/.

[53] Ashworth Briggs, A. J. E., "Free surface interaction of a ' T-foil ' hydrofoil," Ph.D. thesis, University of Tasmania, 2018.

[54] Day, S., Cocard, M., and Troll, M., "Experimental measurement and simplified prediction of T-foil performance for monohull dinghies," *THE 23RD CHESAPEAKE SAILING YACHT SYMPOSIUM*, ANNAPOLIS, MARYLAND, 2019.

[55] Harwood, C. M., Yoon, H., Young, Y. L., and Wright, T., "Dynamic Hydroelastic Response of a Surface-Piercing Strut in Waves," *SNAME Maritime Convention*, Providence, Rhode Island, 2018.

[56] Beaver, B., and Zseleczky, J., "Full scale measurements on a hydrofoil International Moth," *19th Chesapeake Sailing Yacht Symposium, CSYS*, 2009.

[57] Prabahar, N. S. S., Persson, A., and Larsson, L., "Split-Flaps – a Way to Improve the Heel Stability of T-Foil Supported Craft," *Journal of Sailing Technology*, Vol. 7, No. 01, 2022, pp. 1–30. https://doi.org/10.5957/jst/2022.7.1.1, URL https://onepetro.org/JST/article/7/01/1/473113/Split-Flaps-a-Way-to-Improve-the-Heel-Stability-of.

[58] Bonfiglio, L., Royset, J. O., and Karniadakis, G., "Multi-Disciplinary Risk-Adaptive Design of Super-Cavitating Hydrofoil," *2018 AIAA Non-Deterministic Approaches Conference*, American Institute of Aeronautics and Astronautics, Kissimmee, Florida, 2018. https://doi.org/10.2514/6.2018-1177, URL https://arc.aiaa.org/doi/10.2514/6.2018-1177.

[59] Ploe, P., "Surrogate-based optimization of hydrofoil shapes using RANS simulations," Theses, École centrale de Nantes, June 2018. URL https://tel.archives-ouvertes.fr/tel-02050026.

[60] Kenway, G. K. W., Kennedy, G. J., and Martins, J. R. R. A., "Scalable Parallel Approach for High-Fidelity Steady-State Aeroelastic Analysis and Adjoint Derivative Computations," *AIAA Journal*, Vol. 52, No. 5, 2014, pp. 935–951. https://doi.org/10.2514/1.J052255.

[61] Kenway, G. K. W., and Martins, J. R. R. A., "Multipoint High-Fidelity Aerostructural Optimization of a Transport Aircraft Configuration," *Journal of Aircraft*, Vol. 51, No. 1, 2014, pp. 144–160. https://doi.org/10.2514/1.C032150.

[62] pyGeo, "pygeo," , ???? URL https://github.com/mdolab/pygeo.

[63] Secco, N., Kenway, G. K. W., He, P., Mader, C. A., and Martins, J. R. R. A., "Efficient Mesh Generation and Deformation for Aerodynamic Shape Optimization," *AIAA Journal*, Vol. 59, No. 4, 2021, pp. 1151–1168. https://doi.org/10.2514/1.J059491.

[64] Lambe, A. B., and Martins, J. R. R. A., "Extensions to the Design Structure Matrix for the Description of Multidisciplinary Design, Analysis, and Optimization Processes," *Structural and Multidisciplinary Optimization*, Vol. 46, 2012, pp. 273–284. https://doi.org/10.1007/s00158-012-0763-y.

[65] Kenway, G. K., Kennedy, G. J., and Martins, J. R. R. A., "A CAD-Free Approach to High-Fidelity Aerostructural Optimization," *Proceedings of the 13th AIAA/ISSMO Multidisciplinary Analysis Optimization Conference*, Fort Worth, TX, 2010. https://doi.org/10.2514/6.2010-9231.

[66] Luke, E., Collins, E., and Blades, E., "A Fast Mesh Deformation Method Using Explicit Interpolation," *Journal of Computational Physics*, Vol. 231, No. 2, 2012, pp. 586–601. https://doi.org/10.1016/j.jcp.2011.09.021.

[67] ADflow, "ADflow," , ???? URL https://github.com/mdolab/adflow.

[68] Spalart, P., and Allmaras, S., "A One-Equation Turbulence Model for Aerodynamic Flows," *La Recherche Aerospatiale*, Vol. 1, 1994, pp. 5–21.

[69] Yildirim, A., Kenway, G. K. W., Mader, C. A., and Martins, J. R. R. A., "A Jacobian-free approximate Newton–Krylov startup strategy for RANS simulations," *Journal of Computational Physics*, Vol. 397, 2019, p. 108741. https://doi.org/10.1016/j.jcp.2019.06.018.

[70] Lyu, Z., Kenway, G. K. W., and Martins, J. R. R. A., "Aerodynamic Shape Optimization Investigations of the Common Research Model Wing Benchmark," *AIAA Journal*, Vol. 53, No. 4, 2015, pp. 968–985. https://doi.org/10.2514/1.J053318.

[71] Bons, N. P., He, X., Mader, C. A., and Martins, J. R. R. A., "Multimodality in Aerodynamic Wing Design Optimization," *AIAA Journal*, Vol. 57, No. 3, 2019, pp. 1004–1018. https://doi.org/10.2514/1.J057294.

[72] Lee, Y., and Baeder, J., "Implicit hole cutting—a new approach to overset grid connectivity," *16th AIAA Computational Fluid Dynamics Conference*, 2003. https://doi.org/10.2514/6.2003-4128.

[73] Parkin, B. R., Perry, B., and Wu, T. Y., "Pressure Distribution on a Hydrofoil Running near the Water Surface," *Journal of Applied Physics*, Vol. 27, No. 3, 1956, pp. 232–240. https://doi.org/10.1063/1.1722350.

[74] Kenway, G. K. W., and Martins, J. R. R. A., "Buffet-Onset Constraint Formulation for Aerodynamic Shape Optimization," *AIAA Journal*, Vol. 55, No. 6, 2017, pp. 1930–1947. https://doi.org/10.2514/1.J055172.

[75] Young, Y., Wright, T., Yoon, H., and Harwood, C., "Dynamic hydroelastic response of a surface-piercing strut in waves and ventilated flows," *Journal of Fluids and Structures*, Vol. 94, 2020, p. 102899. https://doi.org/10.1016/j.jfluidstructs.2020.102899, URL https://linkinghub.elsevier.com/retrieve/pii/S0889974619305559.

[76] Phillips, A., Cairns, R., Davis, C., Norman, P., Brandner, P., Pearce, B., and Young, Y. L., "Effect of material design parameters on the forced vibration response of composite hydrofoils in air and in water," *Fifth International Symposium on Marine Propulsors*, Espoo, Finland, 2017.

[77] Akcabay, D. T., and Young, Y. L., "Steady and Dynamic Hydroelastic Behavior of Composite Lifting Surfaces," *Composite Structures*, Vol. 227, 2019, p. 111240. https://doi.org/10.1016/j.compstruct.2019.111240.

[78] Akcabay, D. T., and Young, Y. L., "Material anisotropy and sweep effects on the hydroelastic response of lifting surfaces," *Composite Structures*, Vol. 242, 2020, p. 112140. https://doi.org/10.1016/j.compstruct.2020.112140.